Journal of Computational Physics 230 (2011) 5510–5531

Contents lists available at ScienceDirect

Journal of Computational Physics

journal homepage: www.elsevier.com/locate/jcp

Simulation of viscous flows with undulatory boundaries: Part II. Coupling with other solvers for two-fluid computations

Di Yang, Lian Shen *

Department of Civil Engineering, Johns Hopkins University, Baltimore, MD 21218, USA

ARTICLE INFO

Article history:
Received 8 December 2010
Received in revised form 22 February 2011
Accepted 23 February 2011
Available online 12 March 2011

Keywords:
Multi-fluids flow
Wave
Turbulence

ABSTRACT

We extend the direct numerical simulation (DNS) capability developed in [D. Yang, L. Shen, Simulation of viscous flows with undulatory boundaries: Part I. Basic solver, J. Comput. Phys. (submitted for publication)] to the simulation of two-fluid interaction with deformable interface. Two approaches are used to couple the DNS of one fluid with the simulation of another fluid. In the first, the DNS is coupled with a potential-flow based wave solver that uses a high-order spectral (HOS) method. This coupled method is applied to simulate the interaction of turbulent wind with surface waves, including single wave train and broadband wavefield. Validation with previous theoretical and experimental studies shows the accuracy and efficiency of this coupled DNS-HOS method for capturing the essential physics of wind–wave interaction. In the second approach, both of the fluids are simulated by the DNS and are coupled by an efficient iterative scheme, in which the continuity of velocity and the balance of stress are enforced at the interface. The performance of this coupled DNS–DNS method is demonstrated and validated by several test cases including: interfacial wave between two viscous fluids, water surface wave over highly viscous mud flow with interfacial wave, and interaction of two-phase vortex pairs with a deformable interface. Comparison with existing theoretical and numerical results confirms the accuracy of this coupled DNS–DNS method. Finally, this method is applied to study the interaction of air and water turbulence. The nonlinear development of interfacial wave by the excitation of the air and water turbulence, and the wave effect on the instantaneous and statistical characteristics of the turbulence are elucidated.

1. Introduction

Many environmental fluid mechanics problems involve viscous flows interacting with other flows at deformable interfaces. Take wind–wave interaction as an example. As winds blow over water waves, the turbulent windfield is affected by both the kinematic constraint of the alternative concave and convex wave surface and the dynamic distortion by the wave orbital motion [4,39,55,56]. Meanwhile, the wave dynamics is influenced by the wind input mainly through the pressure forcing at the water surface [27,52]. For a mechanistic study of the fundamental physics of wind–wave interaction, it is desirable to develop a numerical tool that is capable of capturing the two-way coupling between the turbulent wind boundary layer and the nonlinear waves.

In the present paper, we investigate the dynamic coupling of the viscous flow solver developed in Yang and Shen [57] (hereinafter referred to as P1) with another flow solver at a deformable interface. In P1, we developed a method for the simulation of Navier–Stokes equations on boundary-fitted grid using an algebraic mapping. The grid follows the curvature of the

* Corresponding author. Tel.: +1 410 516 5033; fax: +1 410 516 7473.
E-mail address: LianShen@jhu.edu (L. Shen).

0021-9991/$ - see front matter © 2011 Elsevier Inc. All rights reserved.
doi:10.1016/j.jcp.2011.02.035

undulatory boundaries with fine resolution near the boundaries to resolve the boundary layers adequately. Both the top and bottom boundaries can be undulatory. While other boundary conditions can be applied at the top and bottom surfaces, we consider a mostly general situation: Neumann conditions with prescribed surface pressure and shear stress at the top boundary that can be used to simulate free-surface flows, and Dirichlet conditions with given surface geometry and surface velocity at the bottom undulatory boundary that can be used to simulate flows such as winds over waves. The method developed in P1 serves as a basic solver, which we use in the present paper to combine with other flow solvers to investigate the multi-fluids flows with deformable undulatory interfaces.

We first consider the coupling of the viscous flow solver with a potential-flow based wave solver to investigate the wind–wave interaction problem. For the waves, we use a high-order spectral (HOS) method [16] that was developed based on the Zakharov formulation [58] and mode-coupling using a pseudo-spectral method. The HOS method is capable of accurately simulating non-breaking surface waves to high orders of wave nonlinearity perturbation [35]. Our scheme for the coupling between wind turbulence and water wave simulations is built on the specific physics of the problem. The air is much lighter than the water, and the air flow sees the water wave surface as a moving wall (see e.g. [12,30]). Meanwhile, the waves evolve subject to the wind forcing, which is mainly through the wave-phase-coherent air pressure applied at the wave surface (see e.g. [46,56]). Therefore, we use a fractional-step method that has alternating prescriptions of surface geometry and velocity for the wind simulation from the wave simulation, and surface pressure for the latter from the former. In our study, this numerical method is applied to situations of winds over monochromatic wave trains as well as over irregular wavefields with broadband wave spectra.

While the above approach captures the essential dynamics of wave nonlinear interaction and evolution, the viscous aspect of the waterside motion is left out. For some other applications such as the vortex dynamics (see e.g. [13,1,7,9]), turbulence transport across the air–sea interface (see e.g. [30,25]), and wind-induce surface drift (see e.g. [54]), we further consider the coupling of two layers of viscous flows with an undulatory interface, each using the solver of P1 as the building block. At the deformable interface, the continuity of velocity and the balance of stress are enforced alternatingly between the two regions through an efficient iterative coupling scheme. Due to the complexity associated with the grid mapping, special care is needed in the momentum equation solver and the treatment of the kinematic and dynamic boundary conditions at the interface.

We remark that in this study we consider the basic flow solver using DNS only. For the application to more realistic problems, large-eddy simulation (LES) can be used, which has been facilitated by the recent developments in subgrid-scale stress and wall function models (see e.g. [6,26,17,2]; also see the review by [8]). Here, we focus on the development of basic numerical coupling scheme, and we limit our discussion to DNS.

This paper is organized as follows. Section 2 presents the coupled DNS-HOS method and demonstrates its application to wind–wave interaction simulation. Section 3 discusses the coupled DNS–DNS method and documents the test cases of two viscous fluids interaction. Finally, conclusions are given in Section 4.

2. Coupling with potential flow wave simulation

To study the interaction between wind turbulence and dynamically evolving surface waves, we couple the DNS method developed in P1 with the potential-flow based wave solver, the HOS method. Numerical details of this coupled method are presented in this section.

2.1. Brief overview of HOS method

The HOS method [16] solves the potential flow wave problem using the Zakharov formulation [58]. The wave motion is described by the surface elevation η and the surface potential Φ^s, which is defined as $\Phi^s = \Phi(x,y,z=\eta(x,y,t),t)$ with Φ being the velocity potential. Here, x and y are horizontal, and z is vertical with $z = 0$ being the mean level of the wave surface. The kinematic and dynamic boundary conditions at the wave surface are written as

$$\eta_t + \nabla_h\eta\cdot\nabla_h\Phi^s - (1+\nabla_h\eta\cdot\nabla_h\eta)\Phi_z(x,y,\eta,t) = 0, \tag{1}$$

$$\Phi^s_t + g\eta + \frac{1}{2}\nabla_h\Phi^s\cdot\nabla_h\Phi^s - \frac{1}{2}(1+\nabla_h\eta\cdot\nabla_h\eta)\Phi_z^2(x,y,\eta,t) = D_\Phi - \frac{P_a}{\rho_w}. \tag{2}$$

Here, $\nabla_h = (\partial/\partial x, \partial/\partial y)$ is the horizontal gradient; g is the gravitational acceleration; ρ_w is the density of water; D_Φ is the wave dissipation (typical models include Φ multiplied by a negative coefficient [53] and eddy viscosity model [49]); P_a is the air pressure at the wave surface; and the subscripts 't' and 'z' denote the partial derivatives with respect to time and vertical coordinate z, respectively.

Using a perturbation series of Φ with respect to wave steepness to order M and the Taylor series expansion about the mean water level $z = 0$ to the corresponding order,

$$\Phi(x,y,z,t) = \sum_{m=1}^{M}\Phi^{(m)}(x,y,z,t), \tag{3}$$

$$\Phi^s(x,y,t) = \sum_{m=1}^{M} \sum_{\ell=0}^{M-m} \frac{\eta^\ell}{\ell!} \frac{\partial^\ell \Phi^{(m)}}{\partial z^\ell}\bigg|_{z=0} \tag{4}$$

and an eigenfunction expansion of each $\Phi^{(m)}$ with N modes,

$$\Phi^{(m)}(x,y,z,t) = \sum_{n=1}^{N} \Phi_n^{(m)}(t)\Psi_n(x,y,z), \quad z \leqslant 0, \tag{5}$$

Eqs. (1) and (2) are rewritten as [16]

$$\frac{\partial \eta}{\partial t} = -\nabla_h \eta \cdot \nabla_h \Phi^s + (1 + \nabla_h \eta \cdot \nabla_h \eta) \times \left[\sum_{m=1}^{M} \sum_{\ell=0}^{M-m} \frac{\eta^\ell}{\ell!} \sum_{n=1}^{N} \Phi_n^{(m)}(t) \frac{\partial^{\ell+1} \Psi_n(x,y,z)}{\partial z^{\ell+1}}\bigg|_{z=0} \right], \tag{6}$$

$$\frac{\partial \Phi^s}{\partial t} = -g\eta - \frac{1}{2}\nabla_h \Phi^s \cdot \nabla_h \Phi^s + D_\Phi - \frac{P_a(x,y,t)}{\rho_w} + \frac{1}{2}(1 + \nabla_h \eta \cdot \nabla_h \eta) \times \left[\sum_{m=1}^{M} \sum_{\ell=0}^{M-m} \frac{\eta^\ell}{\ell!} \sum_{n=1}^{N} \Phi_n^{(m)}(t) \frac{\partial^{\ell+1} \Psi_n(x,y,z)}{\partial z^{\ell+1}}\bigg|_{z=0} \right]^2. \tag{7}$$

In this paper, we consider deep water waves, for which the eigenfunction Ψ in Eq. (5) is

$$\Psi_n(x,y,z) = \exp(|\mathbf{k}_n| z + \imath \mathbf{k}_n \cdot \mathbf{x}), \tag{8}$$

where $\mathbf{k}_n = (k_{xn}, k_{yn})$ is the wavenumber vector and $\imath = \sqrt{-1}$.

In the horizontal directions, periodic boundary conditions are applied. The HOS method uses a Fourier-series-based pseudo-spectral method for the spatial discretization. A fourth-order Runge–Kutta (RK4) scheme is used to advance Eqs. (6) and (7) in time. Complete review of the mathematical formulation, numerical scheme, and validation of the HOS method is provided in [16] and [35].

2.2. Coupling scheme

The DNS is dynamically coupled with the HOS simulation with two-way feedbacks. The focus of our study is on wind turbulence over water waves. We note that the density ratio between water and air is large and thus the wind sees the water surface as a moving wavy wall [12,30]. We also note that the wind forcing on the wave evolution is mainly through the form drag induced by P_a [46,56]. Therefore, at each timestep of the simulation, the wave simulation provides the surface geometry and velocity as Dirichlet boundary conditions for the wind simulation, and the latter provides P_a to the former as the wind forcing (Eq. (7)).

The coupling is performed using a fractional-step method as shown in Fig. 1(a). Because of the large density ratio between water and air, the time scale for the wave to evolve under the wind forcing is much larger than the advection and turnover time scales of the turbulent eddies [4]. Moreover, the HOS method is explicit in time advancing and the DNS is semi-implicit. Therefore, we let HOS simulation advance from timestep (n) to $(n+1)$ first. With the new surface elevation $\eta^{(n+1)}$, the grid mapping for the DNS is performed. The surface values of the velocity (u_s, v_s, w_s) in the DNS obtains from the HOS simulation result as

$$u_s^{(n+1)} = \frac{\partial \Phi^{s(n+1)}}{\partial x} - \frac{\partial \eta^{(n+1)}}{\partial x} \frac{\partial \Phi}{\partial z}\bigg|_{z=\eta}^{(n+1)}, \tag{9}$$

$$v_s^{(n+1)} = \frac{\partial \Phi^{s(n+1)}}{\partial y} - \frac{\partial \eta^{(n+1)}}{\partial y} \frac{\partial \Phi}{\partial z}\bigg|_{z=\eta}^{(n+1)}, \tag{10}$$

$$w_s^{(n+1)} = \frac{\partial \Phi}{\partial z}\bigg|_{z=\eta}^{(n+1)}, \tag{11}$$

where $\partial\Phi/\partial z$ is calculated as (from Eqs. (3)–(5); see [16])

$$\frac{\partial \Phi}{\partial z}\bigg|_{z=\eta} = \sum_{m=1}^{M} \sum_{\ell=0}^{M-m} \frac{\eta^\ell}{\ell!} \sum_{n=1}^{N} \Phi_n^{(m)}(t) \frac{\partial^{\ell+1} \Psi_n(x,y,z)}{\partial z^{\ell+1}}\bigg|_{z=0}. \tag{12}$$

The DNS is then advanced from timestep (n) to $(n+1)$ by the schemes discussed in P1.

We note that in theory multiple iterations are desirable in the coupling of air and water motions in the advancement of each timestep. However, Refs. [32,18,30,25] showed that with one iteration per timestep, the simulation of gas–liquid coupled turbulent flows provides satisfactory results. For the wind–wave interaction problem studied here, the momentum transfer between air and water happens on a time scale that is much larger than the eddy turnover time in turbulence. Therefore, with the small timestep values constrained by the Courant condition, the error of time integration is small and has negligible effect on the flow physics with one iteration.

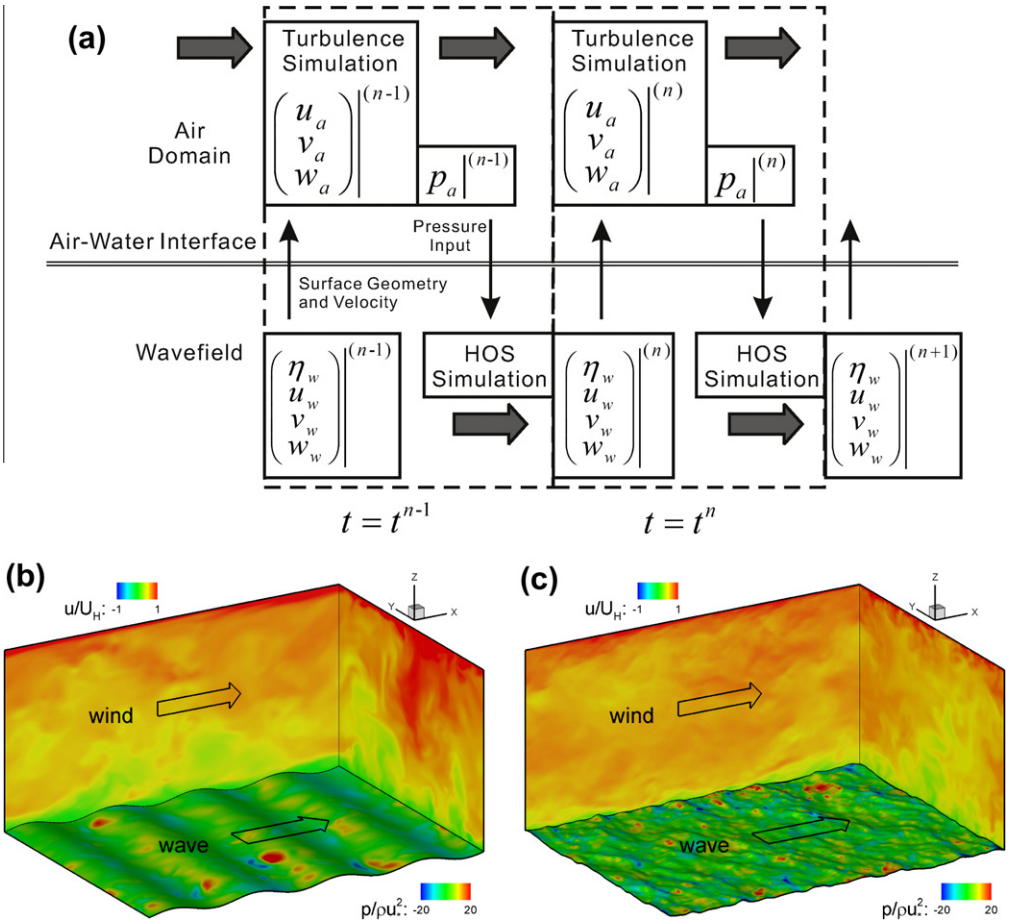

Fig. 1. Illustration of DNS–HOS coupled simulation of the interaction between wind turbulence and water wavefield. Coupling scheme is shown in (a). Simulation examples for wind turbulence over a single wave train and a broadband wavefield are shown in (b) and (c), respectively. In (b) and (c), contours of streamwise velocity are plotted on the two vertical planes and contours of air pressure are plotted on the wave surface.

2.3. Summary of the procedure

The solution procedure of the present coupled DNS-HOS method is summarized as follows:

(i) Update the surface elevation η and surface potential Φ^s from timestep (n) to $(n+1)$ by integrating Eqs. (6) and (7) in time using the RK4 scheme.
(ii) Calculate the wave surface orbital velocity $\mathbf{u}_s^{(n+1)}$ based on Eqs. (9)–(11).
(iii) Calculate the grid mapping for the DNS based on $\eta^{(n+1)}$.
(iv) Perform the DNS for the air turbulence on the $\eta^{(n+1)}$-based grid subject to the Dirichlet velocity boundary condition $\mathbf{u}_s^{(n+1)}$. Details of the DNS method are given in P1.

After step (iv), the values of $P_a^{(n+1)}$ and airside velocity $\mathbf{u}_a^{(n+1)}$ are obtained, and both the wind and wave fields are advanced to timestep $(n+1)$. Steps (i)–(iv) are then repeated for the next timestep and the simulation continues.

2.4. Test results

2.4.1. Growth of single wave train under wind forcing

We first examine the growth of a single wave train under wind forcing, which is of fundamental importance to the study of wind-wave evolution. As a canonical problem, turbulent Couette flow of air over water wave is simulated (Fig. 1(b)) [46,56]. For the air turbulence simulation, the size of the computational domain is $(L_x, L_y, \overline{H}) = (2\pi, 1.5\pi, \pi) = (4\lambda, 3\lambda, 2\lambda)$, where λ is the wavelength. The Reynolds number based on λ and wind friction velocity u_* is $\mathrm{Re}_* = u_*\lambda/\nu_a = 283$, where ν is the kinematic viscosity and the subscript 'a' denotes the air. The water-to-air density ratio is 828. We use a $128 \times 128 \times 129$ grid. The grid is uniformly spaced in the horizontal directions. Here and hereafter, in order to resolve

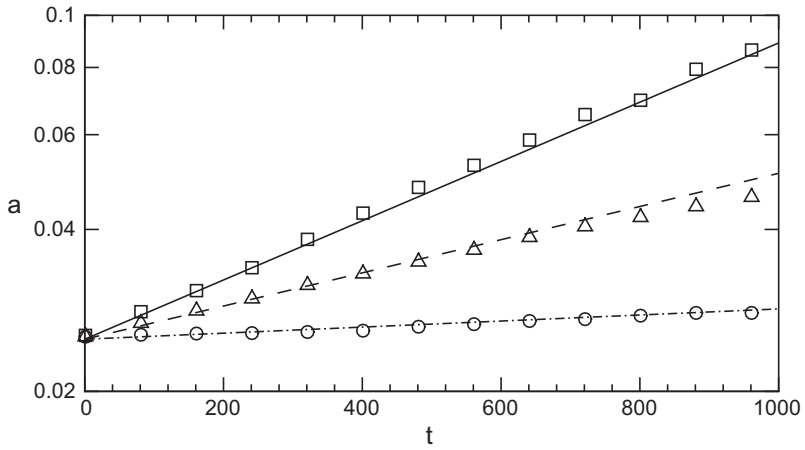

Fig. 2. Evolution of wave amplitude under wind forcing. The evolution of exponentially growing wave amplitude is denoted by lines: —, $c/u_* = 2$; ---, $c/u_* = 5$, and -·-, $c/u_* = 10$. The simulation result is denoted by open symbols: □, $c/u_* = 2$; △, $c/u_* = 5$, and ○, $c/u_* = 10$. The vertical axis is plotted in logarithmic scale.

Table 1
Form drag F_p and growth rate parameter β of water wave under wind forcing.

Wave age (c/u_*)	Form drag (F_p)	Growth rate parameter (β)
2	0.175	35.0
5	0.245	49.0
10	0.090	17.9

the boundary layer, the grid is clustered in the vertical direction unless otherwise indicated. For the simulations in this section and in Section 2.4.2, the vertical grid has the size $\Delta z = 0.002$ near the bottom and top boundaries and $\Delta z = 0.047$ in the middle of the channel, which correspond to 0.42 and 8.45 in wall units, respectively. In the present study the surface wave is progressive, for which the wave phase propagates at the rate of wave phase speed c (defined as the ratio of the wavelength λ to the wave period T [11]). In the present study, three wave phase speeds $c = 2u_*$, $5u_*$ and $10u_*$ are investigated, which belong to the slow wave condition where the momentum transfer from wind to wave is important [4]. The ratio c/u_*, called the wave age, is an important parameter of wind–wave interaction [37,4,56]. The choice of these parameter values is explained and validated in [55,56].

Previous experimental and theoretical studies showed that slow waves grow under wind forcing mainly through the form drag (see the review [4]). In the present study, we start our simulation with an initial wave steepness $ak = 0.1$ (where a is the wave amplitude and $k = 2\pi/\lambda$ is the wavenumber) and record the temporal growth of the wave (Fig. 2). Meanwhile, from the air pressure distribution on the wave surface, the dimensionless form drag per unit area is quantified as [56]

$$F_p = \frac{1}{\lambda}\int_0^{\lambda} \frac{P_a}{\rho_a u_*^2}\frac{d\eta}{dx}dx \tag{13}$$

and the wave growth rate parameter [36] obtains as

$$\beta = \frac{2F_p}{(ak)^2}. \tag{14}$$

Table 1 shows the averaged form drag and growth rate parameter obtained from our simulation. For all of the cases, the form drag is positive, indicating the transfer of momentum from wind to water wave.

The fractional rate of wind energy input to wave per radian advance in phase is [27]

$$\zeta_{wave} = \frac{1}{\omega e}\frac{de}{dt} = \beta\frac{\rho_a}{\rho_w}\left(\frac{u_*}{c}\right)^2, \tag{15}$$

where $e = \rho_w g a^2/2$ is the density of wave energy, and ω is the angular frequency of the wave, and ρ_a is the density of air. Comparison of the ζ_{wave} values obtained by the present method with previous theory and measurements shows good agreement (Fig. 3(c)).

The wind–wave generation theory of Miles [36] shows that the water wave grows exponentially under wind forcing, which has been confirmed by laboratory experiments and field measurements (see the review by [27,4]). From Eq. (15) one can obtain

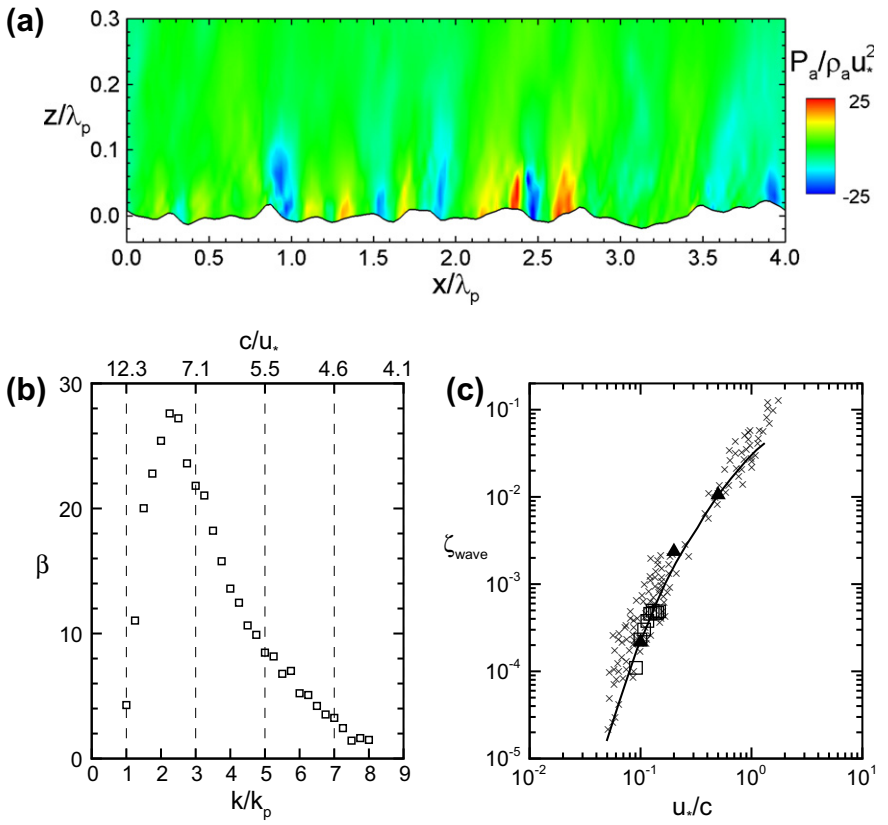

Fig. 3. Wind pressure forcing on a JONSWAP wavefield: (a) instantaneous air pressure distribution on an (x,z)-plane above the wave surface; (b) the wave growth rate parameter β for different modes of the JONSWAP wavefield; and (c) the dependence of ζ_{wave} (defined in Eq. (15)) on the reversed wave age u_*/c compared with the existing measurement data and theoretical prediction. In (c), the field measurement data compiled by [41] is denoted by $\times$; the theoretical prediction by [37] is denoted by —; result for the current single wave train case is denoted by ▲; and result for the current broadband case is denoted by □.

$$a(t) = a_0 \exp\left[\frac{1}{2}\omega\beta\frac{\rho_a}{\rho_w}\left(\frac{u_*}{c}\right)^2 t\right], \tag{16}$$

where a_0 is the wave amplitude at $t = 0$. Using the β values in Table 1, the exponential growth curves given by Eq. (16) are plotted in Fig. 2. Fig. 2 also shows the evolution of wave amplitude directly from the simulation. Good agreement is obtained.

This test indicates the capability of the coupled DNS-HOS method for accurately simulating the wind–wave interaction and providing quantifications of wind-wave evolution. More details of this aspect of results are reported in [31].

2.4.2. Interaction of wind turbulence with broadband water waves

Next, we examine the interaction of wind turbulence with a broadband water wavefield. The computational domain has the size of $(L_x, L_y, \overline{H}) = (2\pi, 1.5\pi, \pi)$, and the grid resolution is $128 \times 128 \times 129$. In the present paper, we limit the simulation to DNS, with the understanding of the potential of extension to LES. Therefore, the Reynolds number is kept at the same relatively low value as in Section 2.4.1, $\mathrm{Re}_* = u_*\lambda/\nu_a = 283$. The water-to-air density ratio is also *828*.

The initial broadband wavefield satisfies the directional wave spectrum

$$S_{2D}(\mathbf{k}) = S(|\mathbf{k}|)\frac{1}{\pi}(\cos^2\theta_D)g^{1/2}|\mathbf{k}|^{-3/2}. \tag{17}$$

Here, $\mathbf{k} = (k_x, k_y)$ is the wavenumber vector as in Eq. (8), and $\theta_D = \tan^{-1}(k_y/k_x)$.

For $S(|\mathbf{k}|)$, we use the one-dimensional spectral function obtained during the Joint North Sea Wave Observation Project (JONSWAP) [22]

$$S(|\mathbf{k}|) = \frac{\alpha}{g^{1/2}|\mathbf{k}|^{5/2}}\exp\left[-\frac{5}{4}\left(\frac{k_p}{|\mathbf{k}|}\right)^2\right]\varepsilon^r, \tag{18}$$

$$r = \exp\left[-\frac{1}{2\sigma^2}\left(\sqrt{\frac{|\mathbf{k}|}{k_p}} - 1\right)^2\right]. \tag{19}$$

Here, the subscript 'p' denotes the spectrum peak; and the constants $\alpha = 0.0121$, $\varepsilon = 3.3$, and

$$\sigma = \begin{cases} 0.07 & |\mathbf{k}| \leqslant k_p, \\ 0.09 & |\mathbf{k}| > k_p. \end{cases} \tag{20}$$

In our simulation, the JONSWAP wavefield has its dominant wave propagating in the $+x$-direction, the same as the mean wind direction. The spectrum peak of the wave satisfies $k_p = 4$ and $c_p/u_* = 12.3$. Fig. 1(c) shows a snapshot of the coupled wind turbulence and wavefield in this simulation.

Fig. 3(a) shows the air pressure distribution in a vertical (x,z)-plane above the JONSWAP wavefield. It shows that for the wave crests, the air pressure is high on the windward face and low on the leeward face, resulting in a form drag and growth of these waves. By applying the spectral analysis to the air pressure distribution and by calculating the corresponding form drag, we obtain the growth rate parameter β for each wave mode. Fig. 3(b) shows the variation of β with k. To help understand its behavior, the value of c/u_* at different k is also indicated on the top of Fig. 3(b). Near the peak wavenumber k_p, the value of β is small, indicating the slow growth of the dominant waves as they belong to the intermediate wave range [4,46,56]. For k around $2k_p$, the wave age is around $c/u_* = 8$ (i.e., the wave age becomes younger), and β increases to reach its maximum. As expected, short waves have higher growth rate than long waves [4].

Note that in Fig. 3(b), for waves near the spectrum tail ($k > 4k_p$), their amplitude is much smaller. Although the values of c/u_* for these waves fall into the slow wave range, their growth rate β does not show large values because of the sheltering effect of the dominant waves on them. We remark that in this paper we use DNS and mainly focus on the discussion of the coupling scheme. For the short waves, their scales resolvable are limited by the smallest turbulence eddies resolved by DNS. LES with advanced wall-layer modeling is clearly desirable. This, however, goes beyond the scope of the present paper. Here we focus on the waves with $k < 4k_p$.

To validate our coupled DNS-HOS method, we compare the value of ζ_{wave} (Eq. (15)) from our simulation with the field measurement data compiled by [41] and the theoretical prediction by [37]. As shown in Fig. 3(c), good agreement is obtained.

In the present simulation, the wavefield not only provides a complex boundary condition for the wind simulation, but also evolves dynamically under the wind pressure forcing (referred to as two-way coupling). To further illustrate their interaction, we perform a comparison simulation with an identical setup, except that we turn off the pressure input in Eq. (7) so that the JONSWAP wavefield evolves freely without the wind forcing (referred to as one-way coupling).

Fig. 4(a) and (b) show a snapshot of the wave surfaces obtained from the two-way and one-way coupling simulations, respectively. Direct observation of the surface geometry indicates that with the wind forcing, the wave surface is rougher than that in the one-way coupling case. This difference can be seen quantitatively from the one-dimensional wave spectrum shown in Fig. 4(c). For the waves with the wavenumber higher than 1.5 k_p, the energy spectral density obtained from the two-way coupling simulation is appreciably larger than that from the one-way coupling simulation.

The results in this section show that the coupled DNS-HOS method can capture the essential physics in the interaction between wind turbulence and broadband water waves. It can serve as a useful research tool for the mechanistic study of wind–wave interaction, which is a subject of our ongoing research.

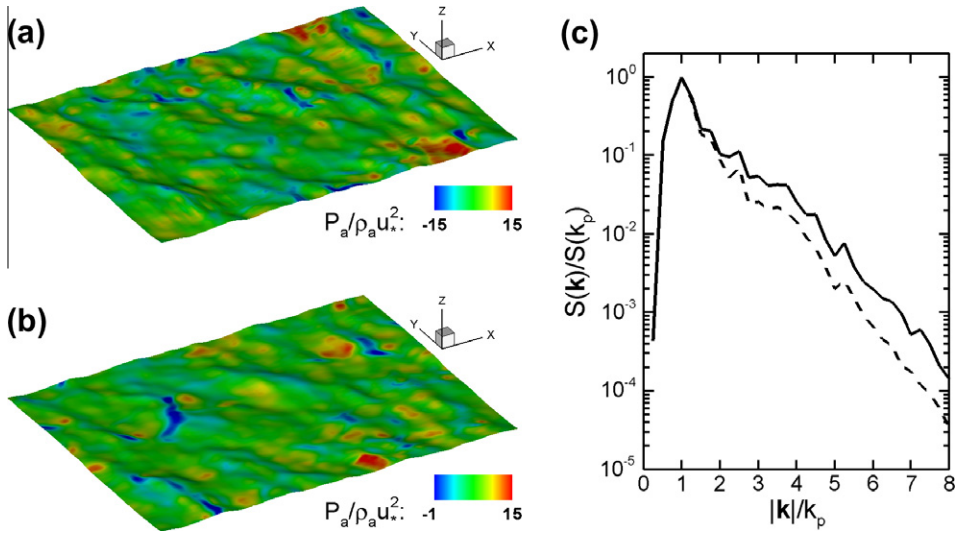

Fig. 4. Illustration of the interaction between wind turbulence and broadband wavefield by the comparison between two-way and one-way coupled simulations. Shown in the left panel is a snapshot of the instantaneous wave surfaces obtained from (a) two-way and (b) one-way coupled simulations. Normalized air pressure contours are plotted at the surfaces. Shown in the right panel is the one-dimensional wave spectrum: —, two-way coupled case; and ---, one-way coupled case.

3. Coupling with another DNS

In Section 2, we have discussed the coupled DNS-HOS method for the study of wind–wave interaction, in which the waterside fluid can be treated as inviscid and is simulated efficiently by the HOS wave solver. For some other applications, the effect of viscosity needs to be considered for both fluids. For this purpose, a coupled DNS–DNS method is developed, which is discussed in this section.

3.1. Numerical scheme

3.1.1. Formulation

As shown in Fig. 5, we consider the interaction between an upper layer of viscous fluid (denoted by the subscript "u") and a lower layer of viscous fluid (denoted by the subscript "l"), separated by a deformable interface. Each layer is simulated by the method introduced in P1. Here we focus on the coupling at the interface $z = \eta = \eta_l = -H'_u$.

At the interface, the velocity is continuous:

$$\mathbf{u}_u = \mathbf{u}_l \quad \text{at } z = \eta. \tag{21}$$

For the stress balance, formulation for the lower layer is given by Eqs. (15*)–(19*) in P1 (hereinafter, the superscript '$\star$' denotes the equations in P1). Here we discuss the upper layer. The tangential stresses at the interface on the upper-layer side are

$$\sigma_{\mathbf{t}i}|_u^{(n+1)} = \left[\rho_u \nu_u C_0^{\mathbf{t}i}\left(C_1^{\mathbf{t}i}\frac{\partial u_u}{\partial \zeta} + C_2^{\mathbf{t}i}\frac{\partial v_u}{\partial \zeta} + C_3^{\mathbf{t}i}\frac{\partial u_u}{\partial \xi} + C_4^{\mathbf{t}i}\frac{\partial v_u}{\partial \varphi} + C_5^{\mathbf{t}i}\frac{\partial u_u}{\partial \varphi} + C_5^{\mathbf{t}i}\frac{\partial v_u}{\partial \xi} + C_6^{\mathbf{t}i}\frac{\partial w_u}{\partial \xi} + C_7^{\mathbf{t}i}\frac{\partial w_u}{\partial \varphi}\right)\right]_{z=\eta}^{(n+1)}, \quad \text{for } i = 1, 2, \tag{22}$$

where

$$\begin{cases} C_0^{\mathbf{t}1} = 1/\sqrt{(1+\eta_x^2+\eta_y^2)(1+\eta_x^2)}, \\ C_1^{\mathbf{t}1} = (1+\eta_x^2+\eta_y^2)(1+\eta_x^2)/(\eta_u + H_u), \\ C_2^{\mathbf{t}1} = (1+\eta_x^2+\eta_y^2)\eta_x\eta_y/(\eta_u + H_u), \\ C_3^{\mathbf{t}1} = -3\eta_x - \eta_x^3 - \eta_x\eta_y^2, \quad C_4^{\mathbf{t}1} = -\eta_x - \eta_x^3 - \eta_x\eta_y^2, \\ C_5^{\mathbf{t}1} = -\eta_y, \quad C_6^{\mathbf{t}1} = 1 - \eta_x^2, \quad C_7^{\mathbf{t}1} = -\eta_x\eta_y, \end{cases} \tag{23}$$

$$\begin{cases} C_0^{\mathbf{t}2} = 1/\sqrt{(1+\eta_x^2+\eta_y^2)(1+\eta_y^2)}, \\ C_1^{\mathbf{t}2} = (1+\eta_x^2+\eta_y^2)\eta_x\eta_y/(\eta_u + H_u), \\ C_2^{\mathbf{t}2} = (1+\eta_x^2+\eta_y^2)(1+\eta_y^2)/(\eta_u + H_u), \\ C_3^{\mathbf{t}2} = -\eta_y - \eta_x^2\eta_y - \eta_y^3, \quad C_4^{\mathbf{t}2} = -3\eta_y - \eta_x^2\eta_y - \eta_y^3, \\ C_5^{\mathbf{t}2} = -\eta_x, \quad C_6^{\mathbf{t}2} = -\eta_x\eta_y, \quad C_7^{\mathbf{t}2} = 1 - \eta_y^2. \end{cases} \tag{24}$$

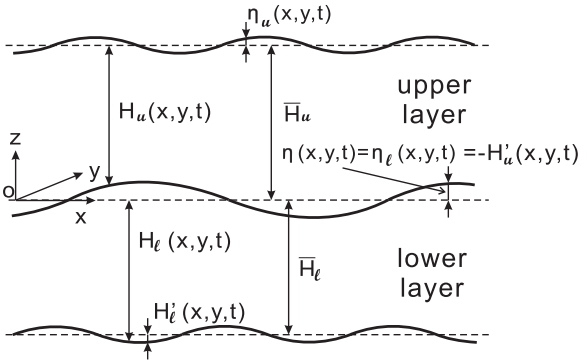

Fig. 5. Illustration of computational domain and geometrical variables in a two-layer viscous fluids coupled simulation.

And the normal stress at the interface on the upper-layer side is

$$\sigma_{\mathbf{n}}|_u^{(n+1)} = \left\{ \rho_u g\eta - p_u + C_0^{\mathbf{n}} \left[C_1^{\mathbf{n}} \frac{\partial u_u}{\partial \xi} + C_2^{\mathbf{n}} \frac{\partial v_u}{\partial \varphi} + C_3^{\mathbf{n}} \left(\frac{\partial u_u}{\partial \varphi} + \frac{\partial v_u}{\partial \xi} \right) + C_4^{\mathbf{n}} \frac{\partial w_u}{\partial \xi} + C_5^{\mathbf{n}} \frac{\partial w_u}{\partial \varphi} \right] \right\}_{z=\eta}^{(n+1)}, \tag{25}$$

where

$$\begin{cases} C_0^{\mathbf{n}} = 2\rho_u \nu_u / (1 + \eta_x^2 + \eta_y^2), \quad C_1^{\mathbf{n}} = -(1 + \eta_y^2), \quad C_2^{\mathbf{n}} = -(1 + \eta_x^2), \\ C_3^{\mathbf{n}} = \eta_x \eta_y, \quad C_4^{\mathbf{n}} = -\eta_x, \quad C_5^{\mathbf{n}} = -\eta_y. \end{cases} \tag{26}$$

In Eqs. (22)–(26), the variables η, η_u, and H_u are defined in Fig. 5, and the subscripts 'x' and 'y' denote partial derivatives.

In the simulation, for the intermediate velocities, Eq. (21) is used in the calculation of the Dirichlet condition of $\hat{\mathbf{u}}_u$ (Eq. (45*)), and Eqs. (22) and (25) are used in the calculation of the Neumann condition of $\hat{\mathbf{u}}_l$ (Eq. (42*)).

Similar to the treatment in Eqs. (37*)–(39*), the terms in Eqs. (22) and (25) are decomposed into velocity related terms and pseudo-pressure related terms (denoted by the superscripts 'v' and '$\wp$', respectively):

$$\sigma_{\mathbf{ti}}|_u^{(n+1)} = \sigma_{\mathbf{ti}}^{\mathrm{v}}|_u^{(n+1)} + \sigma_{\mathbf{ti}}^{\wp}|_u^{(n+1)}, \tag{27}$$

$$\sigma_{\mathbf{n}}|_u^{(n+1)} = \sigma_{\mathbf{n}}^{\mathrm{v}}|_u^{(n+1)} + \sigma_{\mathbf{n}}^{\wp}|_u^{(n+1)}, \tag{28}$$

where

$$\sigma_{\mathbf{ti}}^{\mathrm{v}}|_u^{(n+1)} = \left[\rho_u \nu_u C_0^{\mathbf{ti}} \left(C_1^{\mathbf{ti}} \frac{\partial \hat{u}_u}{\partial \zeta} + C_2^{\mathbf{ti}} \frac{\partial \hat{v}_u}{\partial \zeta} + C_3^{\mathbf{ti}} \frac{\partial \hat{u}_u}{\partial \xi} + C_4^{\mathbf{ti}} \frac{\partial \hat{v}_u}{\partial \varphi} + C_5^{\mathbf{ti}} \frac{\partial \hat{u}_u}{\partial \varphi} + C_5^{\mathbf{ti}} \frac{\partial \hat{v}_u}{\partial \xi} + C_6^{\mathbf{ti}} \frac{\partial \hat{w}_u}{\partial \xi} + C_7^{\mathbf{ti}} \frac{\partial \hat{w}_u}{\partial \varphi} \right) \right]_{z=\eta}^{(n+1)}, \tag{29}$$

$$\begin{aligned} \sigma_{\mathbf{ti}}^{\wp}|_u^{(n+1)} = \Bigg\{ & -\rho_u \nu_u C_0^{\mathbf{ti}} \frac{\Delta t}{\rho_u} \Bigg[C_1^{\mathbf{ti}} \frac{\partial}{\partial \zeta} \left(\frac{\partial \wp_u}{\partial \xi} + \zeta_x \frac{\partial \wp_u}{\partial \zeta} \right) + C_2^{\mathbf{ti}} \frac{\partial}{\partial \zeta} \left(\frac{\partial \wp_u}{\partial \varphi} + \zeta_y \frac{\partial \wp_u}{\partial \zeta} \right) + C_3^{\mathbf{ti}} \frac{\partial}{\partial \xi} \left(\frac{\partial \wp_u}{\partial \xi} + \zeta_x \frac{\partial \wp_u}{\partial \zeta} \right) \\ & + C_4^{\mathbf{ti}} \frac{\partial}{\partial \varphi} \left(\frac{\partial \wp_u}{\partial \varphi} + \zeta_y \frac{\partial \wp_u}{\partial \zeta} \right) + C_5^{\mathbf{ti}} \frac{\partial}{\partial \varphi} \left(\frac{\partial \wp_u}{\partial \xi} + \zeta_x \frac{\partial \wp_u}{\partial \zeta} \right) + C_5^{\mathbf{ti}} \frac{\partial}{\partial \xi} \left(\frac{\partial \wp_u}{\partial \varphi} + \zeta_y \frac{\partial \wp_u}{\partial \zeta} \right) \\ & + C_6^{\mathbf{ti}} \frac{\partial}{\partial \xi} \left(\zeta_z \frac{\partial \wp_u}{\partial \zeta} \right) + C_7^{\mathbf{ti}} \frac{\partial}{\partial \varphi} \left(\zeta_z \frac{\partial \wp_u}{\partial \zeta} \right) \Bigg] \Bigg\}_{z=\eta}^{(n+1)}, \end{aligned} \tag{30}$$

$$\sigma_{\mathbf{n}}^{\mathrm{v}}|_u^{(n+1)} = \left\{ \rho_u g\eta - p_u + C_0^{\mathbf{n}} \left[C_1^{\mathbf{n}} \frac{\partial \hat{u}_u}{\partial \xi} + C_2^{\mathbf{n}} \frac{\partial \hat{v}_u}{\partial \varphi} + C_3^{\mathbf{n}} \left(\frac{\partial \hat{u}_u}{\partial \varphi} + \frac{\partial \hat{v}_u}{\partial \xi} \right) + C_4^{\mathbf{n}} \frac{\partial \hat{w}_u}{\partial \xi} + C_5^{\mathbf{n}} \frac{\partial \hat{w}_u}{\partial \varphi} \right] \right\}_{z=\eta}^{(n+1)}, \tag{31}$$

$$\begin{aligned} \sigma_{\mathbf{n}}^{\wp}|_u^{(n+1)} = \Bigg\{ & -C_0^{\mathbf{n}} \frac{\Delta t}{\rho_u} \Bigg[C_1^{\mathbf{n}} \frac{\partial}{\partial \xi} \left(\frac{\partial \wp_u}{\partial \xi} + \zeta_x \frac{\partial \wp_u}{\partial \zeta} \right) + C_2^{\mathbf{n}} \frac{\partial}{\partial \varphi} \left(\frac{\partial \wp_u}{\partial \varphi} + \zeta_y \frac{\partial \wp_u}{\partial \zeta} \right) + C_3^{\mathbf{n}} \frac{\partial}{\partial \varphi} \left(\frac{\partial \wp_u}{\partial \xi} + \zeta_x \frac{\partial \wp_u}{\partial \zeta} \right) \\ & + C_3^{\mathbf{n}} \frac{\partial}{\partial \xi} \left(\frac{\partial \wp_u}{\partial \varphi} + \zeta_y \frac{\partial \wp_u}{\partial \zeta} \right) + C_4^{\mathbf{n}} \frac{\partial}{\partial \xi} \left(\zeta_z \frac{\partial \wp_u}{\partial \zeta} \right) + C_5^{\mathbf{n}} \frac{\partial}{\partial \varphi} \left(\zeta_z \frac{\partial \wp_u}{\partial \zeta} \right) \Bigg] \Bigg\}_{z=\eta}^{(n+1)}. \end{aligned} \tag{32}$$

We remark that the velocity related terms dominate in Eqs. (27) and (28). For the pseudo-pressure related terms, the value of $\wp^{(n+1)}$ is estimated by $\wp^{(n+1)} = 3\wp^{(n)} - 3\wp^{(n-1)} + \wp^{(n-2)} + O(\Delta t^3)$, as discussed in P1.

With the foregoing numerical treatment for the interfacial stresses, the momentum equations (Eq. (33*)) for the intermediate velocities $\hat{\mathbf{u}}_u$ and $\hat{\mathbf{u}}_l$ can now be coupled and solved iteratively without solving the pressure Poisson equation (Eq. (35*)) together. Eq. (35*) is solved afterwards outside the iteration. The computational cost is thus reduced. Further discussion is given in Section 3.1.2.

We remark that with the numerical framework developed in the present study, it is straightforward to implement the coupling scheme for the transport of heat, chemicals, and contaminants across an interface. For example, the scalar concentration and flux conditions across the interface can be implemented to study the transport of passive scalars in an air–water coupled turbulent flow with a flat interface [30] and an interface with progressive surface waves.

3.1.2. Procedure

The solution procedure of the present coupled DNS–DNS method is summarized here. We remark that as defined before, in the following discussion of this subsection: $f^{(n)}$ and $f^{(n+1)}$ denote the values at timestep (n) and $(n+1)$, respectively; for timestep $(n+1)$, locations of the free surface and the interface are advanced by a second-order Runge–Kutta (RK2) scheme, in which the variable after the first step is denoted by $f^{(n+1)^*}$; after the second step, $f^{(n+1)}$ is obtained (see Section 2.3.2 in P1); at each step of the RK2 scheme, the velocity field is solved by the fractional-step method, in which $\hat{\mathbf{u}}$ denotes the intermediate-step velocity; during iterations, $f^{[m]}$ and $f^{[m+1]}$ denote the values for the previous and current iteration steps, respectively.

The solution procedure is summarized as follows:

(i) Update the surface elevation from $\eta_i^{(n)}$ to $\eta_i^{(n+1)^*}$ ($i = u,l$) based on Eqs. (25*) and (26*), and calculate the corresponding Jacobian matrix Eq. (4*) for the algebraic mapping.

(ii) Solve Eq. (33*) for the upper- and lower-layer fluids iteratively:

(a) For the upper layer, solve $\hat{\mathbf{u}}_u^{[m+1]}$ from Eq. (33*) subject to boundary conditions (37*)–(39*) and (45*). Details of the solver are given in P1. In Eqs. (37*) and (38*), $\sigma_{\mathbf{t}\,\mathrm{i}}|_{\mathrm{external}} = 0$. In Eq. (45*),

$$\mathbf{u}_{\mathrm{b}} = \hat{\mathbf{u}}_l^{[m]} - \frac{\Delta t}{\rho_l}\nabla\left(3\wp^{(n)} - 3\wp^{(n-1)} + \wp^{(n-2)}\right) \quad \text{at } z = \eta_l^{(n+1)^*}. \tag{33}$$

(b) Calculate $\sigma_{\mathbf{ti}}|_u^{[m+1]}$ based on Eq. (27).

(c) For the lower layer, solve $\hat{\mathbf{u}}_l^{[m+1]}$ from Eq. (33*) subject to boundary conditions (37*)–(39*) and (45*). In Eqs. (37*) and (38*), $\sigma_{\mathbf{ti}}|_{\mathrm{external}} = \sigma_{\mathbf{ti}}|_u^{[m+1]}$.

The iteration steps (a)–(c) are repeated until the relative residual errors in Eqs. (21) and (16*) are less than 10^{-6}. The velocities $\hat{\mathbf{u}}_u$ and $\hat{\mathbf{u}}_l$ are then obtained.

(iii) Solve $\wp_u^{(n+1)^*}$ and $\wp_l^{(n+1)^*}$ from Eq. (35*) subject to boundary conditions (47*) and (49*). Details of the solver are given in P1. For the lower layer, the value of $\sigma_{\mathbf{n}}|_{\mathrm{external}}$ is calculated by Eq. (28); for the upper layer, $\sigma_{\mathbf{n}}|_{\mathrm{external}} = 0$.

(iv) Update the velocity from $\hat{\mathbf{u}}_i$ to $\mathbf{u}_i^{(n+1)^*}$ ($i = u,l$) based on Eq. (30*).

(v) Apply the velocity continuity condition Eq. (21) to the upper layer. Apply the tangential stress balance condition Eqs. (18*)–(20*) to calculate the velocity on the ghost point of the lower-layer above the interface (see the points $Nz+1$ and Nz^* in Fig. 2 of P1).

(vi) Update the surface elevation from $\eta_i^{(n+1)^*}$ to $\eta_i^{(n+1)}$ ($i = u,l$) based on Eqs. (27*) and (28*). Repeat steps (ii)–(v) to solve for $\mathbf{u}_i^{(n+1)}$ and $\wp_i^{(n+1)}$ ($i = u,l$).

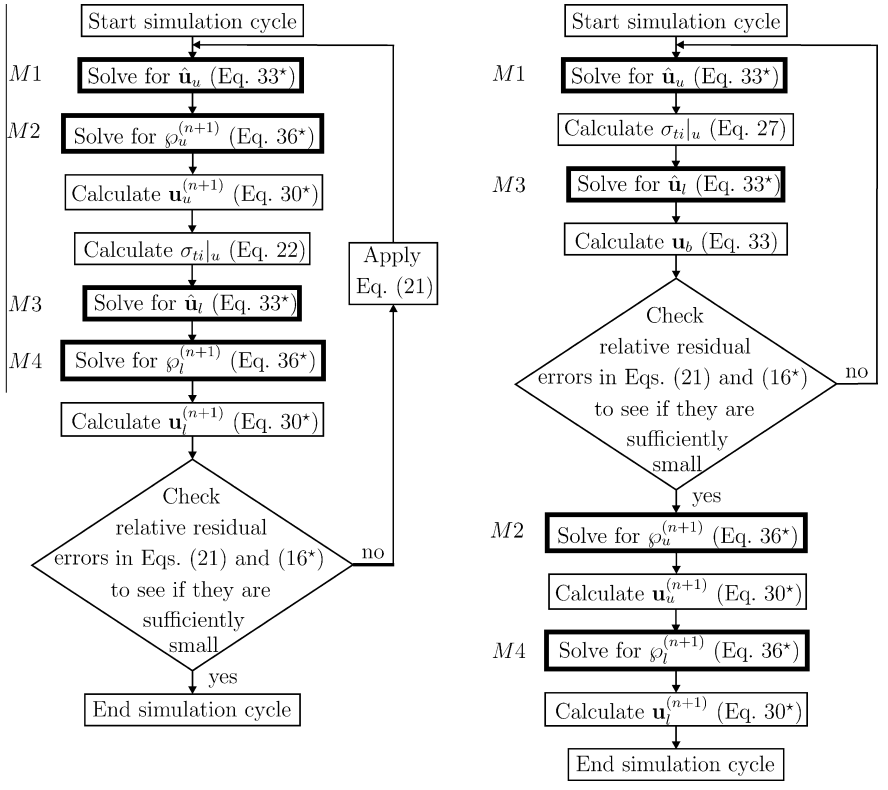

Fig. 6. Flow chart for the DNS–DNS coupled simulation: left panel, previously used coupling approach in the literature (see e.g. [32,25]); right panel, current coupling approach. In each flow chart, the four major simulation steps (named as M_1–M_4) in terms of computational cost are indicated by boxes with thicker boundaries. Here, the superscript '$\star$' denotes the equation in P1.

After the foregoing steps (i)–(vi), the entire two-layer coupled simulation advances from timestep (n) to $(n+1)$.

We note that if the iteration in step (ii) is repeated only once, the current interfacial coupling approach becomes similar to the alternating-advancing approach used in [32,18,30,25]. They showed that for gas–liquid coupled turbulent flow (with large difference in density, $\rho_{gas}/\rho_{liquid} \approx 10^{-3}$), the coupling scheme with one iteration per timestep can provide satisfactory result. This is also the case for the wind–wave interaction problem discussed in Section 2. However, for the problems involving two fluids with comparable densities, e.g., interaction between water wave and mud flow ($\rho_{water}/\rho_{mud} = 0.58 \sim 0.95$ [34]) and two-layer film flow during coating process (density ratio $\approx$1.0 [51,19,20]), the motions of the two fluids are strongly coupled and iteration is thus desired (the effect of density ratio on the two-fluid interaction is discussed in Section 3.2.3).

As shown in Fig. 6, in the simulation there are four major steps in terms of computational cost: M_1 and M_3 that solve the momentum equation for the upper- and lower-layer, respectively; and M_2 and M_4 that solve the pressure Poisson equation. In the previous coupling approach (see e.g. [32,25]), the upper- and lower-layer flows are solved completely first and then iterate with each other, so that M_1–M_4 are all involved during each iteration step (Fig. 6, left panel). Differently, the current approach first solves the momentum equation of the two fluids iteratively; the pressure Poisson equation is solved only after the iteration has converged. As a result, only M_1 and M_3 are now involved in the iteration (Fig. 6, right panel). The current approach thus reduces the computational cost compared with the previous one. This low-cost feature is useful for the statistical study of two-fluid turbulence, which requires long simulation time for statistical convergence.

3.2. Test results

In this section, the performance of the coupled DNS–DNS method is tested by various laminar and turbulent two-fluid flow problems with interfacial waves. Comparison with literature is performed for validation, and good agreement is obtained. We note that the simulation of the onset of an instability such as the Rayleigh–Taylor instability would in general be a good test for a two-fluid coupled method. However, the univalent mapping approach used in the present method impedes such a simulation. Nevertheless, the testing results documented in this subsection provides adequate verification of the present method.

3.2.1. Interfacial wave

We consider the two-dimensional Airy wave at the interface between two fluids, for which the solution by Hendrickson [23] is used. It consists of an irrotational part and a rotational part. The irrotational part is described by the potential functions

$$\begin{cases} \phi_u = aA_1 e^{\imath(2\pi x-\omega t)} e^{-2\pi z} & \text{in the upper layer,} \\ \phi_l = aA_2 e^{\imath(2\pi x-\omega t)} e^{2\pi z} & \text{in the lower layer.} \end{cases} \tag{34}$$

Here, $\imath = \sqrt{-1}$; a is the wave amplitude; and the wavelength of the interfacial wave is set to be $\lambda = 1$ (i.e. $k = 2\pi$). The rotational part of the solution is described by the stream functions

$$\begin{cases} \psi_u = aA_3 e^{\imath(2\pi x-\omega t)} e^{-2\pi k_3 z} & \text{in the upper layer,} \\ \psi_l = aA_4 e^{\imath(2\pi x-\omega t)} e^{2\pi k_4 z} & \text{in the lower layer,} \end{cases} \tag{35}$$

which satisfy the linearized Navier–Stokes equations

$$\begin{cases} \frac{\partial \psi_u}{\partial t} = \nu_u \nabla^2 \psi_u & \text{in the upper layer,} \\ \frac{\partial \psi_l}{\partial t} = \nu_l \nabla^2 \psi_l & \text{in the lower layer.} \end{cases} \tag{36}$$

In Eq. (35), $k_3 = \sqrt{1 - \imath\omega/4\pi^2\nu_u}$ and $k_4 = \sqrt{1 - \imath\omega/4\pi^2\nu_l}$ are complex variables.

Both the top boundary of the upper layer and the bottom boundary of the lower layer are slip free. By applying the kinematic boundary condition and enforcing velocity continuity and stress balance at the interface, the coefficients A_1 through A_4 obtain as

$$\begin{cases} A_1 = \frac{\imath\omega}{2\pi} \frac{k_3 k_4 + k_4 + r_\rho r_\nu + r_\rho r_\nu k_3^2 - 1 + k_3}{(k_4 + r_\rho r_\nu k_3 + r_\rho r_\nu + 1)(k_3 - 1)}, \\ A_2 = -\frac{\imath\omega}{2\pi} \frac{r_\rho r_\nu k_3 k_4 + r_\rho r_\nu k_3 + k_4^2 + 1 + r_\rho r_\nu k_4 - r_\rho r_\nu}{(k_4 + r_\rho r_\nu k_3 + r_\rho r_\nu + 1)(k_4 - 1)}, \\ A_3 = \frac{\omega}{\pi} \frac{k_4 + r_\rho r_\nu}{(k_4 + r_\rho r_\nu k_3 + r_\rho r_\nu + 1)(k_3 - 1)}, \\ A_4 = \frac{\omega}{\pi} \frac{r_\rho r_\nu k_3 + 1}{(k_4 + r_\rho r_\nu k_3 + r_\rho r_\nu + 1)(k_4 - 1)}. \end{cases} \tag{37}$$

Here, $r_\rho = \rho_u/\rho_l$ and $r_\nu = \nu_u/\nu_l$ are respectively the ratios of density and kinematic viscosity between the upper and lower layers. The wave frequency ω is given by the interfacial wave dispersion relationship [28]

$$\omega = \sqrt{2\pi \frac{1 - r_\rho}{1 + r_\rho} + 8\pi^3 \frac{\gamma}{g} \frac{1}{1 + r_\rho}}, \tag{38}$$

where γ is the surface tension.

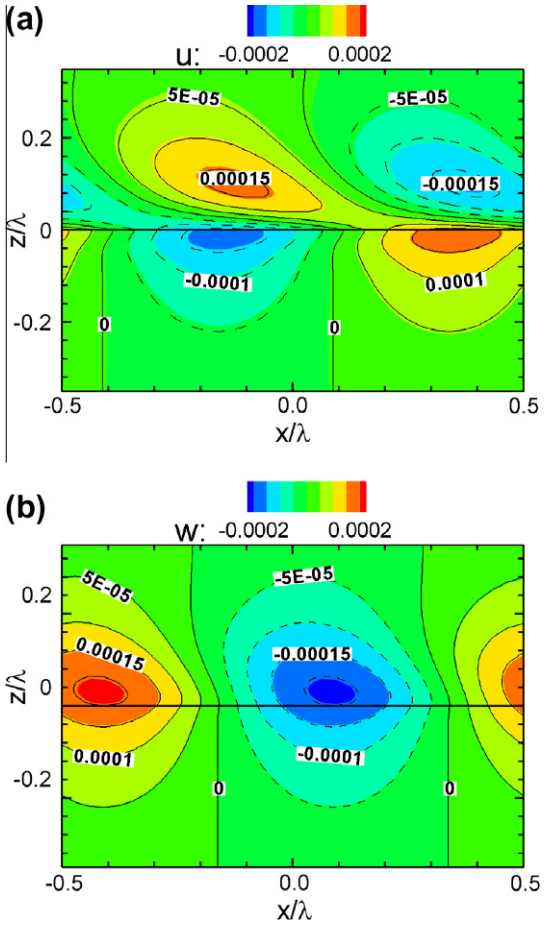

Fig. 7. Velocity components in the two-phase interfacial wave problem: (a) u, and (b) w. Results from the current DNS are shown by the colored contours; those from Eqs. (34) and (35) are shown by lines. The dashed contour lines represent negative values. The contour interval is $5e-5$. Result at $t = 32T$ is plotted, with T being the period of the interfacial wave.

Table 2
Convergence test of interfacial wave for different spatial resolution with a fixed Courant number of 0.5. Definitions of spatial discretization error $\epsilon^s_{i,j}$ and convergence rate m are given in Section 3.1 of P1.

	Grid resolution (1) 32×160 (2) 32×80 (3) 32×40		Convergence rate m
Error in η	$\epsilon^s_{2,1} = 3.61e-6$	$\epsilon^s_{3,2} = 1.24e-5$	1.8

In the test, we set $ak = 0.01, L_x = \overline{H}_u = \overline{H}_l = 1, \mathrm{Fr}^2 = c^2/(g\lambda) = 1.0, \mathrm{We} = (\rho c^2 \lambda)/\gamma = \infty, \mathrm{Re}_l = c\lambda/\nu_l = 2000$, $r_\nu = 10$, and $r_\rho = 0.001$. Fig. 7 shows the simulation result. The velocity distribution in the lower layer is similar to those for the viscous surface wave [28]; in the upper layer, the contours of w extend nearly vertically into the bulk region, while for u there exists a shear, through which the bulk flow is driven by the interfacial wave. The comparison in Fig. 7 shows that our coupled DNS result agrees well with the theoretical solution given by Eqs. 34, 35, 37.

Moreover, we perform spatial and temporal convergence tests by examining the interface deformation η in the same way as in Section 3.3 of P1. For the spatial convergence test, we choose three grids with 32×40, 32×80, and 32×160 evenly distributed points. For the temporal convergence test, we use a fixed spatial resolution of 32×80 and three timesteps of $\Delta t_1 = 0.008$, $\Delta t_2 = 0.01$, and $\Delta t_3 = 0.12$. A reference simulation with a fine timestep of $\Delta t_4 = 0.0008$ is performed. As shown in Tables 2 and 3, a second-order convergence rate is achieved in both space and time.

3.2.2. Water surface wave over highly viscous mud flow with interfacial wave

Next, we examine the interaction between surface waves and interfacial waves below, which has important geophysical applications. One example is the damping of water surface waves by the mud flow at the bottom. Here we consider the

Table 3
Convergence test of interfacial wave for different timesteps with a fixed spatial resolution 32×80. $\Delta t_4 = 0.0008$. Definitions of temporal discretization error $\epsilon^t_{i,j}$ and convergence rate n are given in Section 3.1 of P1.

Timestep	$\Delta t_1 = 0.008$	$\Delta t_2 = 0.01$	$\Delta t_3 = 0.12$	Convergence rate n
Error in η	$\epsilon^t_{1,4} = 2.87e-7$	$\epsilon^t_{2,4} = 4.70e-7$	$\epsilon^t_{3,4} = 6.97e-7$	2.2

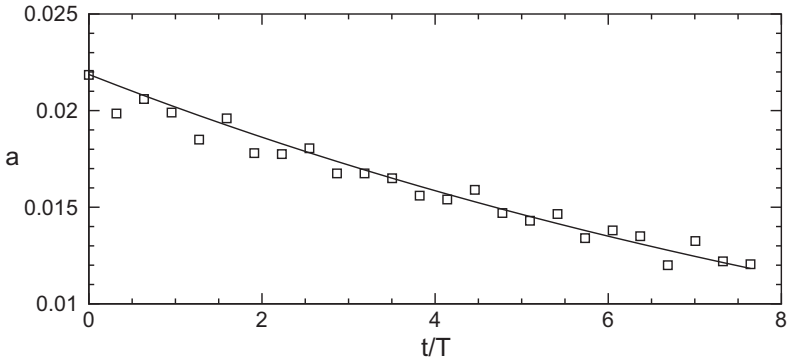

Fig. 8. Decay of amplitude a for water surface wave propagating over a highly viscous mud layer: —, theoretical prediction of [10]; and □, current simulation result.

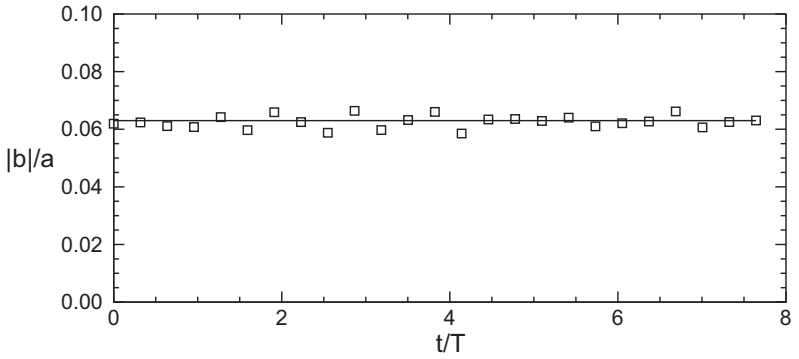

Fig. 9. Ratio of the interface wave amplitude $|b|$ to the free-surface wave amplitude a in the problem of water surface wave propagating over a highly viscous mud layer: —, theoretical prediction of [10]; and □, current simulation result.

model of Dalrymple and Liu [10], in which the interaction between the water surface wave and the interfacial wave at the water–mud interface is solved analytically with the water and the mud being both treated as viscous fluids.

In the theory of [10], both the upper and lower layers of the fluids are assumed to satisfy the linearized two-dimensional Navier–Stokes equations. The elevations of the water surface and the water–mud interface are respectively $\eta_u = ae^{\imath(kx-\omega t)}$ and $\eta_l = be^{\imath(kx-\omega t)}$. Here the surface wave amplitude a and the angular frequency ω are real and known; $k = k_R + \imath k_I$ is the wavenumber with the real part k_R related to the wavelength by $\lambda = 2\pi/k_R$ and the imaginary part k_I indicating the damping rate of the surface wave as it propagates; and the interfacial wave amplitude b is complex.

The solutions for u_i, w_i and p_i $(i = u, l)$ are assumed to have the form of

$$\begin{cases} u_i(x,z,t) = U_i(z)e^{\imath(kx-\omega t)}, \\ w_i(x,z,t) = W_i(z)e^{\imath(kx-\omega t)}, \\ p_i(x,z,t) = P_i(z)e^{\imath(kx-\omega t)}. \end{cases} \tag{39}$$

The solution of $W_i(z)$ can be found in the form of

$$W_u(z) = A\sinh(kz) + B\cosh(kz) + C\exp[\beta_u(z-\overline{H}_u)] + D\exp(-\beta_u z), \tag{40}$$

$$W_l(z) = E\sinh[k(\overline{H}_l + z)] + F\cosh[k(\overline{H}_l + z)] + G\sinh[\beta_l(\overline{H}_l + z)] + H\cosh[\beta_l(\overline{H}_l + z)], \tag{41}$$

where $z = 0$ is the mean interface level; $\beta_i = k^2 - \imath\omega\nu_i^{-1}$; and A–H are complex coefficients. By applying bottom, interfacial, and free-surface boundary conditions, one can obtain ten equations (see Eqs. (13)–(16), (19), and (21)–(24) in [10]) after some algebra. The ten equations are solved to obtain the ten unknowns, i.e., the velocity coefficients A–H, the interface displacement b, and the wavenumber k, which are all complex.

In our test, we set $k_R = 4,\ \lambda = \pi/2,\ L_x = 2\pi,\ \overline{H}_u = 0.491,\ \overline{H}_l = 0.147,\ \mathrm{Fr}^2 = c^2/(g\lambda) = 0.15,\ \mathrm{Re}_u = c\lambda/\nu_u = 11535.0,\ \mathrm{Re}_l = c\lambda/\nu_l = 76.9,\ r_\nu = 6.7 \times 10^{-3}, r_\rho = 0.73$. We simulate the two-dimensional wave–mud interaction problem using a grid of 32×120 points for the upper layer and 32×40 points for the lower layer. The grid is clustered in the vertical direction near the boundaries and interface, with $\Delta z_u|_{min} = 0.001$ and $\Delta z_u|_{max} = 0.009$ for water, and $\Delta z_l|_{min} = 0.001$ and $\Delta z_l|_{max} = 0.008$ for mud. The initial amplitude of the surface wave is set to be $a_0 = 0.022$.

When water wave propagates over a mud layer, an important phenomenon is that the water wave damps much faster than over a rigid bottom. For the parameters chosen above, the theory of [10] predicts a temporal damping rate of $\zeta_I = ck_I = 0.051$, which is much larger than the value of $\zeta_v = 2\nu_u k^2 = 0.004$ if only water viscosity is considered [28]. We perform DNS using the aforementioned parameters. The temporal evolution of the surface wave amplitude shown in Fig. 8 indicates that our simulation agrees with the theory of [10].

We next examine the wave amplitude ratio $|b|/a$, which is an important parameter quantifying the wave–mud interaction [10]. Based on Ref. [10]'s solution, the parameters used in our simulation gives $|b|/a = 0.063$. Fig. 9 shows $|b|/a$ at different time of the simulation, which remains nearly constant in time and agrees well with the theoretical prediction of [10].

We note that there are numerical oscillations in the results shown in Figs. 8 and 9. These oscillations are induced by the standing waves on the free surface and the interface, the magnitude of which is at least one order smaller than that of the dominant wave. Such standing waves are due to the approximations involved in the analytical solution, which is used as the initial condition for the present simulation. They can be suppressed by the relaxation method discussed in [14,15,21]. Such special numerical treatment is beyond the scope of the present study and would lengthen the discussion, and therefore is not included in this paper.

Finally, Fig. 10 shows the profiles of the streamwise and vertical velocity magnitudes ($|u|, |w|$) in both the upper and lower layers. In the lower layer, $|u|$ increases monochromatically as the distance from the bottom increases. In the upper layer, there is a local peak of $|u|$ near the interface, above which the value of $|u|$ first decreases slightly and then increases monochromatically as the height increases. The magnitude of $|w|$, on the other hand, increases monochromatically from the bottom of the lower layer to the surface of the upper layer. Comparison in Fig. 10 shows that the profiles obtained in our simulation agree well with the prediction of [10].

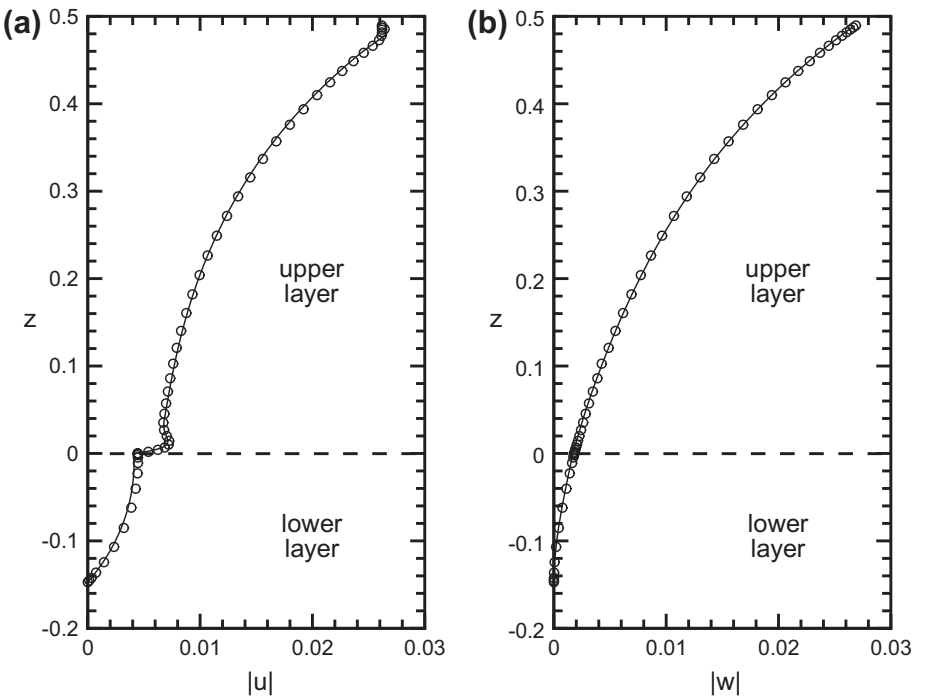

Fig. 10. Profiles of (a) streamwise velocity magnitude $|u|$ and (b) vertical velocity magnitude $|w|$ at $t = 6T$ in the problem of water surface wave propagating over a highly viscous mud layer: ∘, theoretical prediction of [10]; and —, current simulation result.

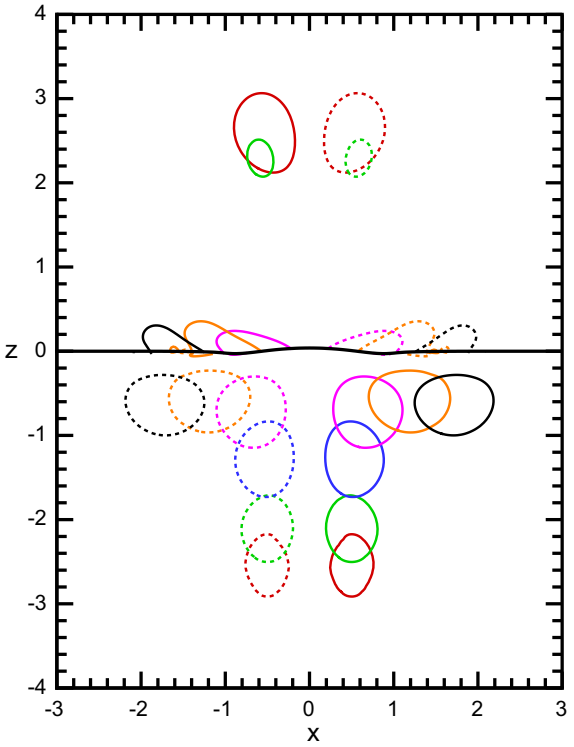

Fig. 11. Evolution of two counter-rotating vortex pairs when approaching the interface: $t = 0.5$, red; $t = 1.0$, green; $t = 2.0$, blue; $t = 3.0$, pink; $t = 4.0$, orange; and $t = 5.0$, black. The contour lines of the transverse vorticity $\omega_y = \pm 4.0$ are plotted for each time. Dashed contour lines indicate negative values. Only the interface at $t = 3.0$ is plotted for illustration. Evolution of the interface elevation is shown in Fig. 12. (For interpretation of the references to colour in this figure legend, the reader is referred to the web version of this article.)

3.2.3. Interaction of two-phase vortex pairs with a deformable interface

Next, we consider the interaction of two vortex pairs with the interface between two layers of fluids. Initially, the interface is flat, and there exist two pairs of counter-rotating vortices in the upper and lower layers that are mirror-imaged about the interface. The simulation of the lower layer is the same as the single-phase simulation in Section 3.4 of P1, except for the difference between the free surface in P1 and the interface here. For the upper layer simulation, we set $r_\nu = \nu_u/\nu_l = 10$, $r_\rho = \rho_u/\rho_l = 0.02$; same domain size as that of the lower layer is used. For this two-dimensional problem, in both fluids a 256×129 grid is used, which is clustered vertically near the interface with the minimum and maximum grid spacing $\Delta z_{min} = 0.005$ and $\Delta z_{max} = 0.086$, respectively.

For comparison, we perform a simulation with identical parameters using a level-set method (LSM), which treats the two layers as a one-fluid system with varying density and viscosity [44]. The fluid interface is implicitly represented by a level-set function ϕ^{LS}, which denotes the signed distance from the interface. In the LSM, ϕ^{LS} is advected by the flow and a reinitialization procedure is performed to help preserve its property as the distance function (see e.g. [47]). For spatial discretization, we use a second-order finite-difference scheme on a staggered grid. A 256×256 grid is used, which is uniformly spaced in the horizontal direction, but clustered in the vertical direction with $\Delta z_{min} = 0.006$ near the interface and $\Delta z_{max} = 0.186$ in the bulk flow. The time integration is realized through a second-order Runge–Kutta scheme, with the pressure obtained by a projection method. Numerical details and validations of the current LSM approach can be found in [23,55].

Figs. 11–13 show the results. Fig. 11 shows the evolution of the vortex pairs in the two fluids. Each vortex pair move towards the interface due to the self induction of the counter rotation. In the lower layer, the pair of vortices maintain their relative position till $t = 4.0$ and start departing horizontally as they approach the interface [1]. The vortex pair in the upper layer, on the other hand, are dissipated quickly and lose their strength after $t = 1.0$. After $t = 4.0$, interfacial vortices are generated in the upper layer because of the induction by the vortex pair in the lower layer.

During the above process, the interfacial deformation is dominated by the motion of the heavy fluid in the lower layer. As shown in Fig. 12(a), at $t = 2.0$ the interface in the middle ($x = 0$) is pushed up by the upwelling flow between the vortices (due to the symmetry of the problem as shown in Fig. 11, only half of the domain of $x > 0$ is plotted). As the vortices approach the interface ($t = 3.0$), the interface is further pushed up in the middle, but is rolled downward on the outer sides of the vortices to form a concave. At $t = 3.5$, the vortices depart from each other and the interface between them falls back; meanwhile, the interface at $|x| > 1.5$ moves upward. The comparison of the present method and the LSM in Fig. 12(left) shows good agreement.

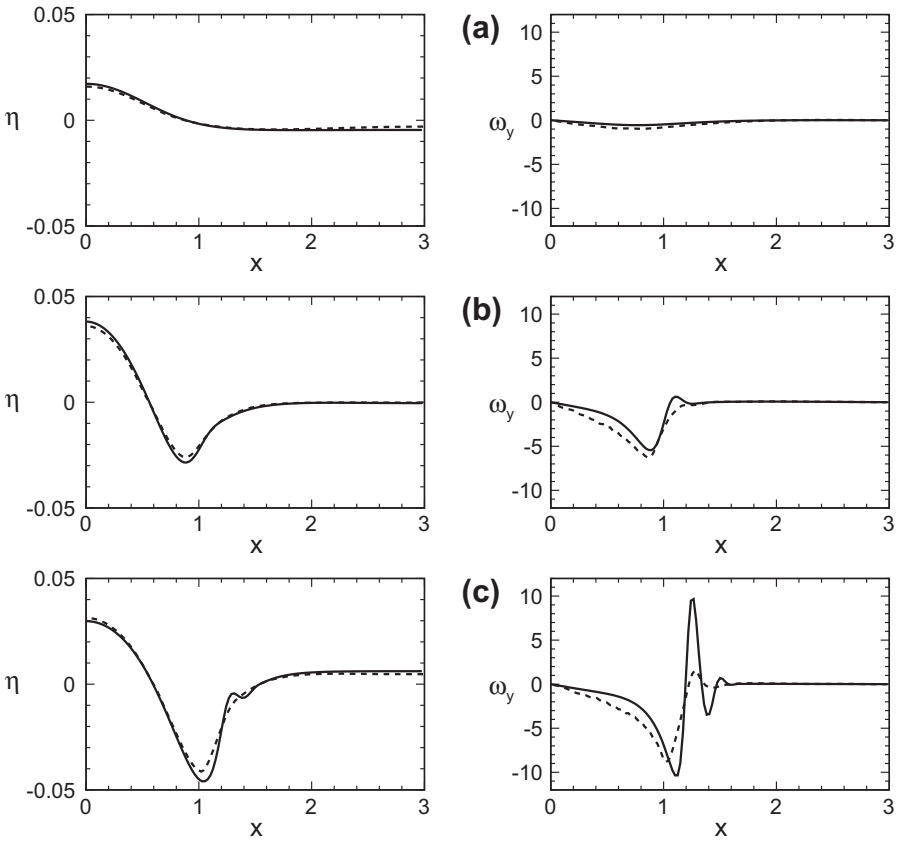

Fig. 12. Profiles of the interface elevation η (left panel) and the transverse vorticity ω_y (right panel) at $t =$: (a) 2.0, (b) 3.0, and (c) 3.5, during the interaction of two vortex pairs with a deformable interface. Results from two different methods are compared: —, current simulation result; and —, simulation result by a level-set method. Due to the symmetry of the problem as shown in Fig. 11, only half of the domain of $x > 0$ is plotted.

Fig. 12 (right) shows the distribution of transverse vorticity ω_y at the interface. The present method provides consistent vorticity distribution as the LSM does at $t = 2.0$ (Fig. 12(a)) and $t = 3.0$ (Fig. 12(b)). However, when the vortices get close to the interface and the secondary vortices are generated (at $t = 3.5$ as shown in Fig. 12(c)), the present method shows larger surface vorticity and more finely resolved secondary vortices than the LSM does.

The difference at $t = 3.5$ can also be seen from the vorticity contours shown in Fig. 13. In both simulations, the primary vortex in the lower layer is clearly shown. The vortex in the upper layer, on the other hand, is dissipated quickly. In Fig. 13(a), the secondary vortices (vortices S_1–S_3) at the interface in the lower layer are resolved by the present method. In the result by the LSM (Fig. 13(b)), the strongest secondary vortex S_1 is resolved, but the vortices S_2 and S_3 are not captured. We remark that the surface profile with two depressed areas (named as 'double scar') shown in Fig. 12(c) and Fig. 13(a) has also been observed in previous studies (see e.g. [38]). At the free surface the vorticity can be approximated as $\omega_y \approx -2\kappa_s u_s$ [33,3], where $\kappa_s = \eta''/(1+\eta'^2)^{(3/2)}$ is the signed surface curvature and u_s is the surface tangential velocity. The changing sign of the surface curvature around the double scar causes the changing sign of the surface vorticity, which can be seen clearly in Fig. 12(c) and Fig. 13(a). Furthermore, in the present study the surface is considered to be clean (no surfactant). If there is surfactant, the surface vorticity would be enhanced due to the shear stress associated with the unevenly distributed surfactant [5,50]. Meanwhile, surfactant in general eradicates the spatial variation of the surface elevation; however, when the surface tension is weak, the local large gradient of surfactant concentration may result in the steepening of the free surface and generate a Reynolds ridge as discussed in the literature [43,1,24,42].

In summary, the comparison between the present method and the LSM shows consistent result for the interfacial deformation. However, the present method captures the interfacial vortices with more details, while the LSM yields much smoother results near the interface because of the Continuum Surface Force approach used in the interfacial jump conditions [47,44,23]. This result supports the recent LSM development by using sharp interface treatment (e.g., [29] and [48], among others), and indicates the importance of resolving the fine flow structure near the interface.

To examine the effect of density ratio on the two-fluid interaction, we also perform two additional simulations with identical setup except that the density ratio is reduced to $r_\rho = 0.001$ and 0 (i.e. the case discussed in Section 3.4 of P1). Fig. 14 shows the comparison of the interfacial profiles of η and ω_y at $t = 3.5$ for $r_\rho = 0.02$, 0.001, and 0. For the three cases

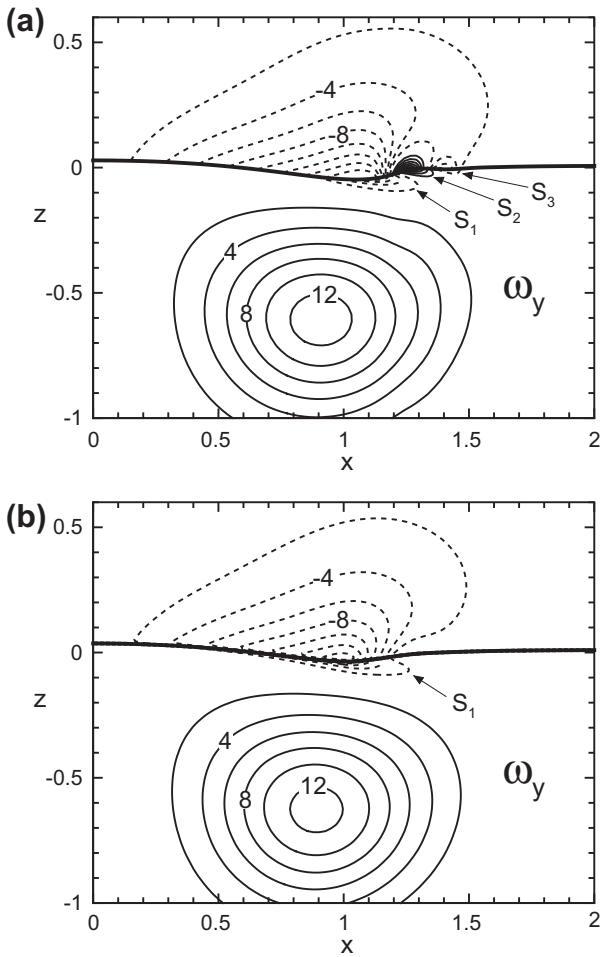

Fig. 13. Comparison of the distribution of the transverse vorticity ω_y at $t = 3.5$ during the interaction of two vortex pairs with a deformable interface obtained by: (a) the current method; and (b) a level-set method. The secondary interfacial vortices S_1–S_3 are indicated in the plot. Dashed contour lines indicate negative values. Due to the symmetry of the problem as shown in Fig. 11, only half of the domain of $x > 0$ is plotted.

considered here, the difference in η is small (Fig. 14(a)). The interfacial profile of ω_y, however, shows obvious difference between $r_\rho = 0.02$ and 0. Because the upper-layer fluid is relatively heavier for $r_\rho = 0.02$, the interface appears less slippery for the lower-layer fluid than the free-slip one of $r_\rho = 0$, resulting in negative ω_y (opposite to the primary vortex in the bulk flow of the lower layer) at the interface between $x = 0$ and *1*. This difference is similar to the difference between no-slip and free-slip boundaries discussed in [42,45]. When r_ρ decreases from 0.02 to 0.001, the distribution of ω_y becomes much closer to that for $r_\rho = 0$. For the case of small r_ρ, the simplification of treating the upper layer as vacuum thus provides a good approximation.

3.2.4. Interaction of air and water turbulence with deformable interface

After testing the DNS–DNS coupling for the laminar flow problems in Sections 3.2.1, 3.2.2, 3.2.3, we next investigate a coupled air–water turbulent flow. As a canonical problem, an air–water Couette flow is simulated. The bottom of the water domain is set to be no-slip and flat; the top boundary of the air domain is set to be flat and a constant shear stress is applied on it. This flow was studied by [30,25] for the special situation of the air–water interface being flat. In the present simulation, the interface is allowed to have deformation.

We match the simulation parameters with those in [30,25] except for the Froude number (in the present simulation, $\mathrm{Fr}^2 = u_{*w}^2/(g\overline{H}_w) = 3.45 \times 10^{-3}$, where u_{*w} is the friction velocity on the waterside; in [30], $\mathrm{Fr}^2 = 0$ corresponding to a flat interface). The air and water sub-domains have the size of $(L_x, L_y, \overline{H}) = (2\pi, \pi, 1)$. The air-to-water density ratio is $r_\rho = \rho_a/\rho_w = 1.2 \times 10^{-3}$ and the viscosity ratio is $r_\nu = \nu_a/\nu_w = 12.7$. In this subsection, the subscripts '*a*' and '*w*' stand for the airside and waterside, respectively. The Weber number is $\mathrm{We} = \rho_w u_{*w}^2 \overline{H}_w/\gamma = 2.69 \times 10^{-5}$. The friction Reynolds number on the waterside is $\mathrm{Re}_w^* \equiv u_{*w}\overline{H}_w/\nu_w = 120$. The friction Reynolds number on the airside is [30]

$$\mathrm{Re}_a^* = r_\rho^{-1/2} r_\nu^{-1} \mathrm{Re}_w^* \approx 271. \tag{42}$$

We use a $128 \times 128 \times 129$ grid for the air and water sub-domains. The grid is clustered in the z-direction near the interface and the top and bottom boundaries, with $\Delta z_{min} = 7.50 \times 10^{-4}$ and $\Delta z_{max} = 1.49 \times 10^{-2}$. A convergence test in [30] using a coarse $64 \times 64 \times 97$ grid and a fine $256 \times 256 \times 256$ grid shows that the current $128 \times 128 \times 129$ grid is adequate and necessary for the DNS.

We use the fully developed air and water turbulence field data from [30] as the initial condition for the current simulation. The interface is initially flat. Because of the excitation by the turbulence from the waterside and the airside, the interface deforms shortly after the simulation starts. Fig. 15 shows two typical development stages. At an early time $t^+ = tu_{*w}^2/\nu_w = 2.4$, small-scale interface deformations are generated (Fig. 15(a)). They consist of bumps and streaks, which are mostly associated with the splats and streamwise vortices in the waterside turbulence (see e.g. Section 3.5 of P1). The comparison between the interface elevation and the air pressure distribution on the interface shows no clear correlation, suggesting that the role of air pressure in the interface deformation development is insignificant at this early stage. We remark that the present problem is different from the wind-wave generation problem, in which the wind turbulence triggers waves on initially calm water (see e.g. [40,36]).

As the interface continues to evolve, large-scale interfacial waves are generated (Fig. 15(b)). At $t^+ = 204.5$ shown in the figure, the dominant interfacial wave has wavenumber $k = 4$ in the x-direction. The air pressure distribution shows apparent wave phase dependence, with high pressure on the windward side of the wave crest and low pressure on the leeward side.

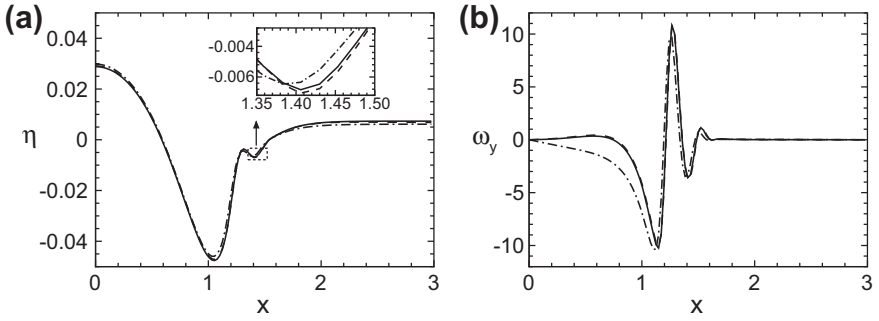

Fig. 14. Effect of density ratio r_ρ on the two-phase vortex pair interaction: (a) interface deformation and (b) interfacial transverse vorticity at $t = 3.5$. Results for three different density ratios are compared: -·-, $r_\rho = 0.02$; —, $r_\rho = 0.001$; and —, $r_\rho = 0$. Due to the symmetry of the problem as shown in Fig. 11, only half of the domain of $x > 0$ is plotted.

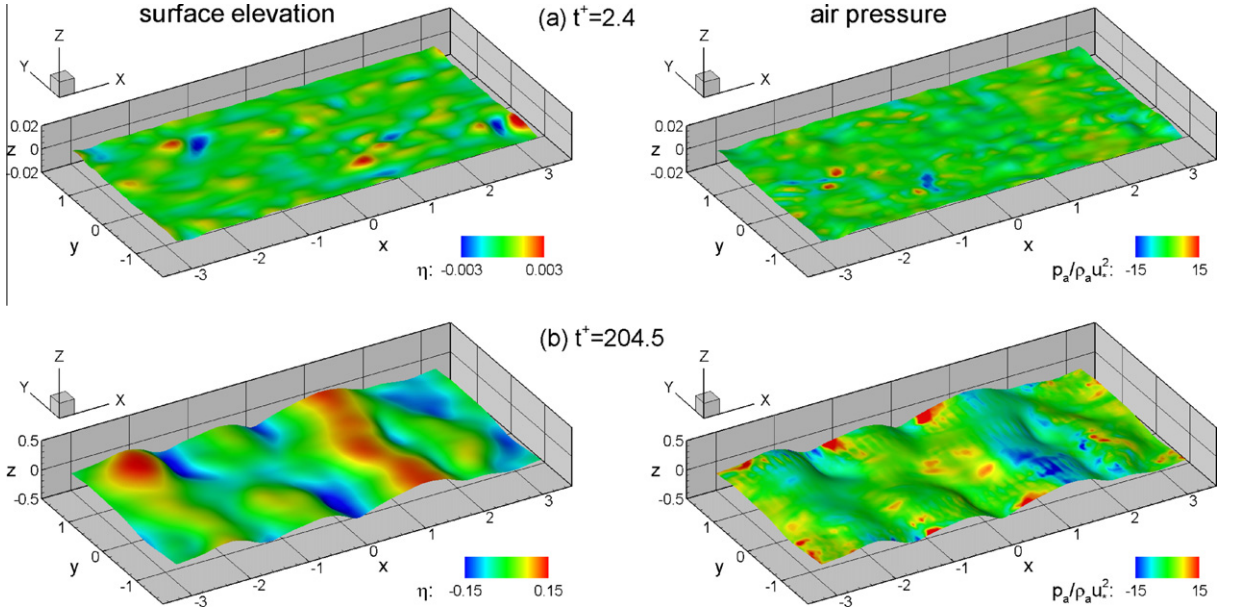

Fig. 15. Snapshots of instantaneous air–water interface at (a) $t^+ = 2.4$ and (b) $t^+ = 204.5$. On the left panel of each plot, the contours of surface elevation η are shown at the interface; on the right panel, the contours of air pressure p_a are shown at the interface.

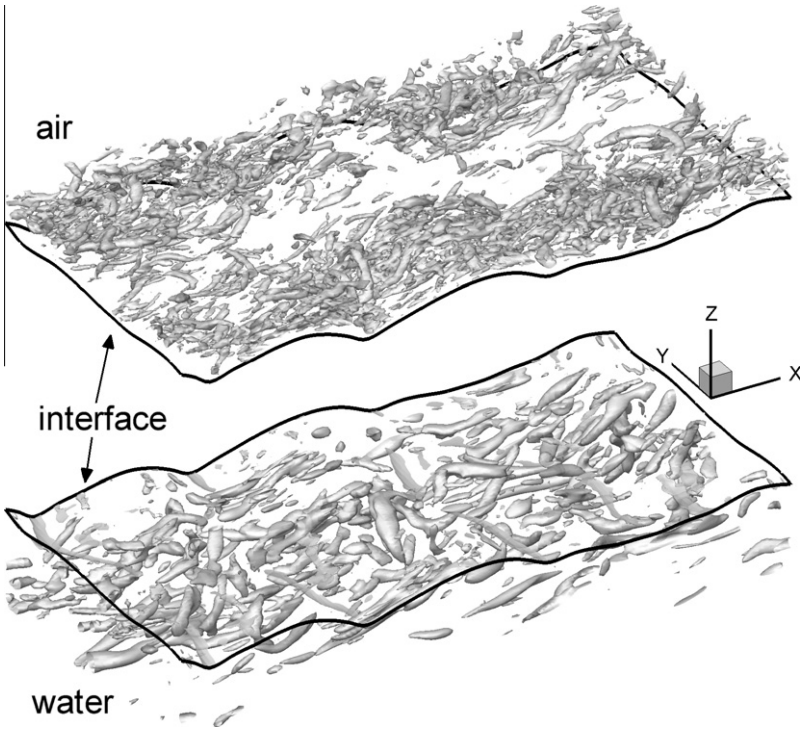

Fig. 16. Instantaneous vortical structures in air–water coupled Couette flow with interfacial waves. Airside vortices are plotted on the upper panel, and waterside vortices are plotted on the lower panel. The mean flow is along the +*x*-direction in both fluids, and the interfacial waves propagate in the +*x*-direction as well. The vortices are represented by the iso-surface of $\lambda_2 = -0.8$. Here λ_2 is the second largest eigenvalue of the tensor $\mathbf{S}^2 + \mathbf{\Omega}^2$, where $\mathbf{S}$ and $\mathbf{\Omega}$ are respectively the symmetric and antisymmetric parts of the velocity gradient tensor $\nabla\mathbf{u}$.

This pressure difference results in appreciable flux of momentum and energy from the air turbulence to the waves. Note that in Fig. 15(b), the small scale variation (with the scale of several grid points) of the surface pressure is not a sign of numerical instability. They are caused by the small scale airside vortices near the interface.

Fig. 16 shows a snapshot of the vortical structures in air and water. On the airside, the distribution of the vortices depends on the wave phase. Note that the interfacial wave has considerable transverse variation (Fig. 15(b)). As a result, the airside vortices also have transverse variation and are more intense over large-amplitude wave surface, consistent with the discussion in [55]. On the waterside, the vortices are mainly along the streamwise direction. Their sizes are larger compared with those on the airside because of the smaller friction Reynolds number in water [30]. Meanwhile, the vortices on the waterside do not show large transverse variation as on the airside. Such phenomenon is consistent with the simulation result of [30], who showed that the waterside vortices are more persistent in their evolution. In the present deformable surface case, they are less affected by the local interfacial wave. The airside vortices are swept over the surface rapidly and are strongly affected by the disturbance induced by the interfacial wave.

The influence of the interfacial waves on the turbulence statistics is shown in Fig. 17 through the comparison with the flat-interface results of [25]. For the current case with deformable interface, the mean value of a variable is obtained by averaging over a plane of constant ζ and over time, where ζ is the vertical coordinate in the computational space (details of the coordinate transformation is given in P1). In Fig. 17, $\bar{z}$ denotes the mean physical height of the grid points with constant ζ.

Note that the visual discontinuity of the upper- and lower-layer profiles at the interface is because the variables are normalized by the parameters in their own layer. Fig. 17(a) shows that the airside mean velocity in the present deformable interface case is apparently smaller than that in the flat interface case, because of the extra momentum loss to the interfacial wave; due to the continuity of velocity across the interface, the mean velocity on the waterside of the interface is also smaller in the present simulation. The turbulence intensity $q\left(=\sqrt{u'^2_{rms}+v'^2_{rms}+w'^2_{rms}}\right)$ is larger in the deformable interface case than in the flat interface case (Fig. 17(b)) on both the airside and the waterside, because of the disturbance of the interfacial waves on the turbulence field. Fig. 17(c) shows that the vorticity fluctuation intensity $q_\omega\left(=\sqrt{\omega'^2_{x,rms}+\omega'^2_{y,rms}+\omega'^2_{z,rms}}\right)$ is also larger in the deformable interface case, especially in the near interface region of the airside.

The simulation result in this section shows that the present coupled DNS–DNS method captures the nonlinear development of the interfacial wave. It can serve as a simulation tool for the study of interfacial wave phenomena in environmental and engineering applications, e.g., small-scale wind–wave–water interaction and two-phase channel flows. This method

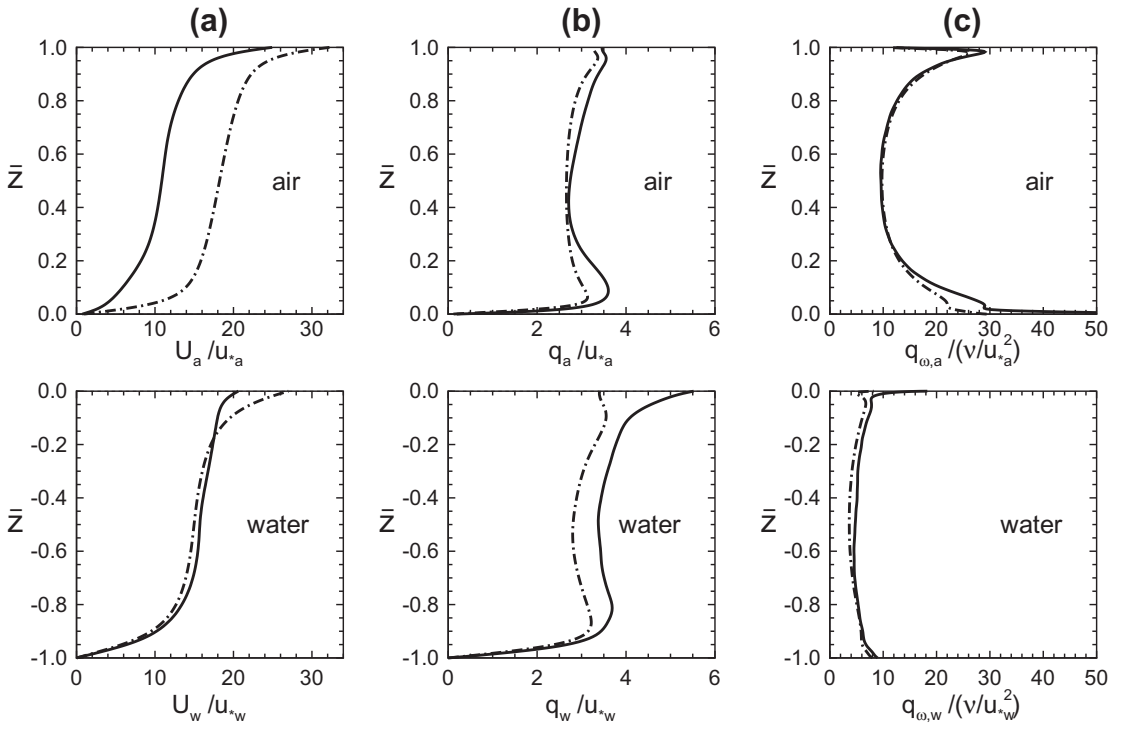

Fig. 17. Profiles of normalized (a) mean streamwise velocity U, (b) total velocity fluctuation intensity $q = \sqrt{u_{rms}^2 + v_{rms}^2 + w_{rms}^2}$, and (c) total vorticity fluctuation intensity $q_\omega = \sqrt{\omega_{x,rms}^2 + \omega_{y,rms}^2 + \omega_{z,rms}^2}$ in air–water coupled Couette flow: —, deformable interface case with $Fr^2 = 3.45 \times 10^{-3}$; -·-, flat interface case with $Fr^2 = 0$. In each fluid, the quantities are normalized by its own u_* value.

resolves the wave-induced variation in the turbulence structures. It provides useful information for the mechanistic study of two-fluid turbulence with deformable interface.

4. Conclusions

This paper extends the DNS method developed in [57] to the simulation of two-fluid flow with deformable interface of finite amplitude. We have developed two coupled simulation methods aiming at different applications.

The first method is developed for the study of interaction between wind turbulence and water waves. For this application, the waterside motion is treated as potential flow and is simulated by an efficient HOS method. The DNS of wind turbulence and the HOS simulation of surface waves are coupled dynamically through a two-way feedback scheme. Validation is performed by simulating wind turbulence over both single wave train and irregular wavefield with broadband spectrum. Comparison of wind pressure forcing and wave growth rate shows quantitative agreement with previous theory and measurements. Results of the broadband wave case indicate that the coupled DNS–HOS method can serve as a useful tool for the mechanistic study of the complex wind–wave interaction problem. We emphasize that extension of DNS to LES is necessary for the study of more realistic problems, and the present paper serves as an initial step for the investigation of some of the numerical coupling issues.

The second method is developed as a general simulation tool for the study of two viscous flows interaction with deformable interface. In this method, the motions for both of the fluids are calculated by the DNS method of P1. This coupled DNS–DNS method, though computationally more expensive than the coupled DNS–HOS method, takes the viscosity of both fluids into account and is able to study the interfacial vortex dynamics and turbulence transport. In this method, both the continuity of velocity and the balance of stress are enforced at the deformable interface through a modified iterative scheme, which is computationally more efficient than those in the literature. Extensive comparison and validation are performed for a series of test cases including two-phase interfacial wave, water surface wave over mud flow, and two-phase vortex pairs interacting with deformable interface. Good agreement with previous theories and simulations are obtained. Particularly, the result for the vortex pair case indicates the high accuracy of the current boundary-fitted method in resolving the interfacial flow structures.

Finally, we apply the coupled DNS–DNS method to simulate the interaction of air and water turbulence. Finite amplitude interfacial waves are generated in the interaction process. The interfacial deformation is found to develop nonlinearly with

distinct features at different stages of evolution. Comparison with the flat interface case shows that the effect of interfacial waves on the turbulence statistics is significant, which the present coupled DNS–DNS method can capture accurately.

Acknowledgements

This research is supported by Office of Naval Research. We thank the referees for their helpful comments.

References

[1] P. Ananthakrishnan, R.W. Yeung, Nonlinear interaction of a vortex pair with clean and surfactant-covered free surfaces, Wave Motion 19 (1994) 343.
[2] W. Anderson, C. Meneveau, A large-eddy simulation model for boundary-layer flow over surfaces with horizontally resolved but vertically unresolved roughness elements, Boundary-Layer Meteor. 137 (2010) 397.
[3] G.K. Batchelor, An Introduction to Fluid Dynamics, Cambridge University Press, 1967.
[4] S.E. Belcher, J.C.R. Hunt, Turbulent flow over hills and waves, Annu. Rev. Fluid Mech. 30 (1998) 507.
[5] L.P. Bernal, A. Hirsa, J.T. Kwon, W.W. Willmarth, On the interaction of vortex rings and pairs with a free surface for varying amounts of surface active agent, Phys. Fluids A 2001 (1989) 1.
[6] E. Bou-Zeid, C. Meneveau, M. Parlange, A scale-dependent Lagrangian dynamic model for large eddy simulation of complex turbulent flows, Phys. Fluids 17 (2005) 025105.
[7] R. Bouffanais, Simulation of shear-driven flows: Transition with a free surface and confined turbulence, Ph.D. Thesis, Swiss Federal Institute of Technology, Schweizerische Nationalbibliothek NB 001515598, 2007.
[8] R. Bouffanais, Advances and challenges of applied large-eddy simulation, Comput. Fluids 39 (2010) 735.
[9] R. Bouffanais, D.L. Jacono, Unsteady transitional swirling flow in the presence of a moving free surface, Phys. Fluids 21 (2009) 064107.
[10] R.A. Dalrymple, P.L.F. Liu, Waves over soft muds: a two-layer fluid model, J. Phys. Oceanog. 8 (1978) 1121.
[11] R.G. Dean, R.A. Dalrymple, Water Wave Mechanics for Engineers and Scientists, World Scientific, 1991.
[12] V. De Angelis, P. Lombardi, S. Banerjee, Direct numerical simulation of turbulent flow over a wavy wall, Phys. Fluids 9 (1997) 2429.
[13] D.G. Dommermuth, The laminar interactions of a pair of vortex tubes with a free surface, J. Fluid Mech. 246 (1993) 91.
[14] D. Dommermuth, The initialization of vortical free-surface flows, J. Fluids Eng. 95 (1994) 116.
[15] D. Dommermuth, The initialization of nonlinear waves using an adjustment scheme, Wave Motion 307 (2000) 32.
[16] D.G. Dommermuth, D.K.P. Yue, A high-order spectral method for the study of nonlinear gravity waves, J. Fluid Mech. 184 (1987) 267.
[17] S. Dupont, F. Gosselin, C. Py, E. De Langre, P. Hemon, Y. Brunet, Modelling waving crops using large-eddy simulation: comparison with experiments and a linear stability analysis, J. Fluid Mech. 652 (2010) 5.
[18] M. Fulgosi, D. Lakehal, S. Banerjee, V. De Angelis, Direct numerical simulation of turbulence in a sheared air–water flow with a deformable interface, J. Fluid Mech. 482 (2003) 319.
[19] P. Gao, X.-Y. Lu, Effect of surfactants on the inertialess instability of a two-layer film flow, J. Fluid Mech. 591 (2007) 495.
[20] P. Gao, X.-Y. Lu, Mechanism of the long-wave inertialess instability of a two-layer film flow, J. Fluid Mech. 608 (2008) 379.
[21] X. Guo, L. Shen, On the generation and maintenance of waves and turbulence in simulations of free-surface turbulence, J. Comput. Phys. 228 (2009) 7313.
[22] K. Hasselmann, T.P. Barnett, E. Bouws, H. Carlson, D.E. Cartwright, K. Enke, J.A. Ewing, H. Gienapp, D.E. Hasselmann, P. Kruseman, A. Meerburg, P. Müller, D.J. Olbers, K. Richter, W. Sell, H. Walden, Measurements of wind-wave growth and swell decay during the Joint North Sea Wave Project (JONSWAP), Dtsch. Hydrogr. Z. Suppl. A 8 (1973) 95.
[23] K.L. Hendrickson, Navier–Stokes simulation of steep breaking water waves with a coupled air–water interface, Ph.D. Thesis, Massachusetts Institute of Technology, 2004.
[24] A. Hirsa, W.W. Willmarth, Measurements of vortex pair interaction with a clean or contaminated free surface, J. Fluid Mech. 25 (1994) 259.
[25] A. Kermani, Numerical study of turbulence and scalar transport process in free-surface and multi-phase flows, Ph.D. Thesis, Johns Hopkins University, 2010.
[26] J. Kleissl, V. Kumar, C. Meneveau, M.B. Parlange, Numerical study of dynamic Smagorinsky models in large-eddy simulation of the atmospheric boundary layer: validation in stable and unstable conditions, Water Resour. Res. 42 (2006) W06D10.
[27] G.J. Komen, L. Cavaleri, M. Donelan, et al, Dynamics and Modelling of Ocean Waves, Cambridge University Press, 1994.
[28] H. Lamb, Hydrodynamics, Dover, 1932.
[29] X.-D. Liu, R.P. Fedkiw, M. Kang, A boundary condition capturing method for Poisson's equation on irregular domains, J. Comput. Phys. 160 (2000) 151.
[30] S. Liu, A. Kermani, L. Shen, D.K.P. Yue, Investigation of coupled air–water turbulent boundary layers using direct numerical simulations, Phys. Fluids 21 (2009) 062108.
[31] Y. Liu, D. Yang, X. Guo, L. Shen, Numerical study of pressure forcing of wind on dynamically evolving water waves, Phys. Fluids 22 (2010) 041704.
[32] P. Lombardi, V. De Angelis, S. Banerjee, Direct numerical simulation of near-interface turbulence in coupled gas–liquid flow, Phys. Fluids 8 (1996) 1643.
[33] M.S. Longuet-Higgins, Mass transport in water waves, Proc. R. Soc. Lond. A 245 (1953) 535.
[34] C.C. Mei, M. Krotov, Z. Huang, A. Huhe, Short and long waves over a muddy seabed, J. Fluid Mech. 643 (2010) 33.
[35] C.C. Mei, M. Stiassnie, D.K.P. Yue, Theory and Applications of Ocean Surface Waves Part 2: Nonlinear Aspects, World Scientific, 2005.
[36] J.W. Miles, On the generation of surface waves by shear flows, J. Fluid Mech. 3 (1957) 185.
[37] J.W. Miles, Surface-wave generation revisited, J. Fluid Mech. 256 (1993) 427.
[38] S. Ohring, H.J. Lugt, Interaction of a viscous vortex pair with a free surface, J. Fluid Mech. 227 (1991) 47.
[39] M. Ortega-Sánchez, S. Bramato, E. Quevedo, C. Mans, M.A. Losada, Atmospheric-hydrodynamic coupling in the nearshore, Geophys. Res. Lett. 35 (2008) L23601.
[40] O.M. Phillips, On the generation of waves by turbulent wind, J. Fluid Mech. 2 (1957) 417.
[41] W.J. Plant, A relationship between wind stress and wave slope, J. Geophys. Res. 87 (1982) 1961.
[42] T. Sarpkaya, Vorticity, free suface, and surfactants, Annu. Rev. Fluid Mech. 28 (1996) 83.
[43] J.C. Scott, Flow beneath a stagnant film on water: the Reynolds ridge, J. Fluid Mech. 283 (1982) 116.
[44] J. Sethian, P. Smereka, Level set methods for fluid interfaces, Annu. Rev. Fluid Mech. 35 (2003) 341.
[45] L. Shen, X. Zhang, D.K.P. Yue, G.S. Triantafyllou, The surface layer for free-surface turbulent flows, J. Fluid Mech. 386 (1999) 167.
[46] P.P. Sullivan, J.C. McWilliams, C.-H. Moeng, Simulation of turbulent flow over idealized water waves, J. Fluid Mech. 404 (2000) 47.
[47] M. Sussman, E. Fatemi, P. Smereka, S. Osher, And improved level set method for incompressible two-phase flows, Comput. Fluids 27 (1998) 663.
[48] M. Sussman, K.M. Smith, M.Y. Hussaini, M. Ohta, R. Zhi-Wei, A sharp interface method for incompressible two-phase flows, J. Comput. Phys. 221 (2007) 469.
[49] Z. Tian, M. Perlin, W. Choi, Energy dissipation in two-dimensional unsteady plunging breakers and an eddy viscosity model, J. Fluid Mech. 655 (2010) 217.
[50] G. Tryggvason, J. Abdollahi-Alibeik, W.W. Willmarth, A. Hirsa, Collision of a vortex pair with a contaminated free surface, Phys. Fluids A 1215 (1992) 4.
[51] S.J. Weinstein, K.J. Ruschak, Coating flows, Annu. Rev. Fluid Mech. 36 (2004) 29.

[52] L. Cavaleri, J.-H.G.M. Alves, F. Ardhuin, A. Babanin, M. Banner, K. Belibassakis, M. Benoit, M. Donelan, J. Groeneweg, T.H.C. Herbers, P. Hwang, P.A.E.M. Janssen, T. Janssen, I.V. Lavrenov, R. Magne, J. Monbaliu, M. Onorato, V. Polnikov, D. Resio, W.E. Rogers, A. Sheremet, J. McKee Smith, H.L. Tolman, G. van Vledder, J. Wolf, I. Young, The WISE Group, Wave modelling—The state of the art, Prog. Oceanogr. 75 (2007) 603.
[53] G. Wu, Direct simulation and deterministic prediction of large-scale nonlinear ocean wave-field, Ph.D. Thesis, MIT, 2004.
[54] J. Wu, Prediction of near-surface drift currents from wind velocity, J. Hydraul. Div. ASCE 99 (1973) 1291.
[55] D. Yang, L. Shen, Characteristics of coherent vortical structures in turbulent flows over progressive surface waves, Phys. Fluids 21 (2009) 125106.
[56] D. Yang, L. Shen, Direct-simulation-based study of turbulent flow over various waving boundaries, J. Fluid Mech. 650 (2010) 131.
[57] D. Yang, L. Shen, Simulation of viscous flows with undulatory boundaries: Part I. Basic solver, J. Comput. Phys. 230 (2011) 5488–5509.
[58] V.E. Zakharov, Stability of periodic wave of finite amplitude on the surface of a deep fluid, J. Appl. Mech. Tech. Phys. 2 (1968) 190.